PROPERTIES OF TiO_2 THIN FILMS AND A STUDY OF THE TiO_2-GaAs INTERFACE

Final Report on
NASA Grant No.
NSG 1202-S1

June 1977

Chung-Yih Chen and Michael A. Littlejohn

North Carolina State University
Electrical Engineering Department
Box 5275, Raleigh, N. C. 27607

ABSTRACT

CHEN, CHUNG-YIH. Properties of TiO_2 Thin Films and a Study of the TiO_2-GaAs Interface. (Under the direction of MICHAEL ANTHONY LITTLEJOHN).

Titanium dioxide (TiO_2) films prepared by chemical vapor deposition (CVD) are investigated in this study for the purpose of the application in the GaAs-MISFET. An ellipsometer, an X-ray diffractometer, and a UV-visible spectrophotometer are employed to measure the film thickness and optical constants, to determine the crystallinity of the TiO_2 films, and to measure the density-of-state energy gap, respectively. The crystallinity of the TiO_2 films is dependent upon the deposition temperature in such a way that the degree of crystallization increases with the deposition temperature. Refractive indexes varying from 1.84 to 2.1, depending on the crystallinity of the films, are computed from the experimental data. The optical gaps, based on the results of the optical absorption, are 3.22 eV and 3.90 eV for the amorphous and anatase films, respectively.

The current-voltage (I-V) study, utilizing an Al-TiO_2-Al MIM structure, reveals that the d-c conduction through the TiO_2 film is dominated by the bulk-limited Poole-Frenkel emission mechanism. The dependence of the resistivity of the TiO_2 films on the deposition environment is also shown. A high frequency (1 MHz) capacitance-voltage (C-V) system is used to investigate the electrical properties of the TiO_2-GaAs interface by measuring the C-V characteristic of an Al-TiO_2-GaAs MIS capacitor. The results of the C-V study indicate that an inversion layer in an n-type substrate can be achieved in the MIS capacitor if the TiO_2 films are deposited at a temperature higher than 275°C. Nevertheless, the etching susceptibilities of the TiO_2 films decrease as

the degree of crystallization is increased. A process of low temperature deposition followed by the pattern definition and a higher temperature annealing is suggested for device fabrications. A flat-band voltage of 2.0 V and a relative dielectric constant of about 50 are also obtained. Fast surface state densities are substantially high and in the order of $10^{13}/cm^2$ eV.

A model, based on the assumption that the surface state densities are continuously distributed in energy within the forbidden band gap, is proposed to interpret the lack of an inversion layer in the Al-TiO_2-GaAs MIS structure with the TiO_2 films deposited at 200°C. This model is in good agreement with the experimental results. This study indicates that a p-channel GaAs-MISFET can be successfully fabricated if the good properties of the 400°C TiO_2-GaAs interface can be utilized.

TABLE OF CONTENTS

LIST OF TABLES

LIST OF FIGURES

LIST OF FIGURES (continued)

LIST OF FIGURES (continued)

Page

1. INTRODUCTION AND LITERATURE REVIEW

1.1 Introduction

The use of silicon dioxide (SiO_2) thin films in solid state device technology has been wide spread for several reasons. The passivation of surface layers, masking against diffusion, and the provision of an active insulating layer in metal-insulator-semiconductor (MIS) devices are among the very common uses. The extensive use of SiO_2 in silicon technology can also be partly attributed to the fact that SiO_2 can be readily grown on silicon by thermal oxidation.

Almost at the same time that silicon technology received wide attention, gallium-arsenide (GaAs) has received similar consideration. The major features of GaAs compared to Si as an electronic material are: (1) greater energy gap allowing operation at higher temperature [1], (2) high electron mobility giving theoretically higher frequency response [2], and (c) a direct band gap providing much shorter recombination time [3].

In spite of the features described above, no satisfactory inversion channel GaAs metal-insulator-semiconductor field effect transitor (MISFET) was realized at the time of starting this research. A prominent problem encountered in GaAs technology is that GaAs decomposes and arsenic atoms evaporate from the surface at a temperature higher than 700°C [4]. These formidable shortcomings make thermal oxidation difficult. Many efforts have been made to study the low temperature oxidation processes, such as chemical vapot deposition (CVD), sputtering, anodic oxidation, and plasma oxidation. A variety of dielectric films, such as SiO, SiO_2, Al_2O_3, Si_3N_4, and Ge_3N_4, have also been studied for this purpose [4]-[8]. Most of the dielectric film - GaAs interfaces investigated so far have the

common problem that the interface state density is very high (on the order of $10^{12}/cm^2$-eV) and the inversion layer is generally hard to achieve, probably due to the high density of surface states or high d-c conduction in the dielectric films.

The interest of this work centers around titanium dioxide (TiO_2) for several reasons. Titanium dioxide is a dense material which is ideally suited for metallurgical protection of GaAs surfaces during ion implantation. The high density of the TiO_2 [9] supposedly allows constituents of the material to be prevented from diffusing into the oxide film. Furthermore, TiO_2 has a reported dielectric constant as high as 150 [10]. MIS structures using a high permittivity insulating material will enjoy the high capacitive density on the one hand, and a relatively large value of transconductance on the other hand [11]. Due to the various favorable reasons mentioned above and due to the fact that no prior work on the TiO_2 - GaAs interface properties has been reported, the primary goal of this research effort is the study of the optical and electrical properties of pyrolytically deposited TiO_2 and the TiO_2 - GaAs interface.

The second chapter deals with the theoretical background related to the understanding of this study. Among the theories presented, the capacitance-voltage (C-V) characteristic of the MIS capacitor and the mechanisms of d-c conduction are well understood. However, certain topics concerning the band model of non-crystalline solids still remain controversial [12]. The experimental techniques are treated in the third chapter. X-ray diffraction and optical absorption are designated to study the structure and optical band gap of the films. In view of the study of the electrical properties of the interfaces, the most convenient and widely used technique is the capacitance-voltage (C-V) and current-voltage

(I-V) characteristics of the MIS structures. The experimental results are then presented in the fourth chapter. Finally, the summary, conclusion, and the recommendations are given in the fifth chapter.

1.2 Dielectric Films for MIS Structures

In order to achieve acceptable device properties, any insulating material used in the metal-insulator-semiconductor (MIS) structure will have to satisfy a number of requirements. As far as the dielectric properties are concerned, one would like to have a material with a relatively high dielectric constant, and it should have a high breakdown strength. It is also important that the MIS structure should remain stable under operational stress, e.g., high temperature or high electric field. There exist two kinds of instabilities; one is due to ion migration, the other is due to charge injection and trapping [13]. It is generally required that the dielectric films be an effective barrier against ion drift, particularly sodium ions. The dielectric films with large band gaps are usually believed to be able to decrease to some extent the possibility of charge injection. It is known that because of disruption of the periodicity of the semiconductor lattice and because of defects at the insulator-semiconductor interface, electronic states will be introduced into the forbidden gap of the semiconductor. Such electronic states are referred to as interface states. From the point of view of device application, interfaces with low interface state density are preferable because interface states usually act as surface recombination centers [11]. The chemical nature of the material should be such that it can be readily etched in liquid etchants at near room temperature. With some refractory materials (e.g., silicon carbide, rutile) one encounters difficulty in this respect. In

considering the device reliability one also has to exclude the water soluable compounds.

In reviewing the dielectric properties of binary compounds, Harrop and Campbell [14] found a number of empirical rules. Only those of our interest will be discussed here.

(1) The energy gap (E_g) of the dielectric materials tends to increase with decreasing mean atomic weight of the constituents. Thus, in a number of oxides of metals with the same valence, the energy gap will increase with decreasing atomic weight of the metal atoms. In light of this rule, one concludes that materials with large band gap will particularly be found among the oxides and nitrides of lighter elements.

(2) The dielectric constant (ϵ_r) of an insulator tends to increase with the mean atomic weight of the components of the compound. This rule implies that it will be unlikely to find materials with both large ϵ_r and large E_g.

(3) Moreover, films with large dielectric constant generally lead to the possibility of high conduction.

Following these rules, Harrop and Campbell concluded that among the large possible number of binary combinations, only a limited number are worth further consideration for application in metal-insulator-semiconductor devices. Magnesium oxide (MgO), aluminum oxide (Al_2O_3), silicon dioxide (SiO_2), silicon oxide (SiO), aluminum nitride (AlN), boron nitride (BN), and silicon nitride (Si_3N_4) are believed to have large band gaps (E_g > 5 eV) with low loss, while bismuth oxide (Bi_2O_3), hafnium oxide (HfO_2), tungsten oxide (WO_3), and tantalum oxide (Ta_2O_5) are among the group showing large dielectric constant (ϵ_r > 10) but

somewhat smaller band gaps. The reason why titanium dioxide (TiO_2), which shows a band gap of the order of 3.8 eV and ε_r of 150, was rejected in this list is not known.

A fairly complete review of the properties of the dielectric materials has been presented by Balk [15] in 1975. A variety of dielectric materials such as Al_2O_3, Si_3N_4, SiO_2, SiO, and Ta_2O_5 have attained a level of practical application in some particular aspects. Readers who are interested in Al_2O_3 [16,17], Si_3N_4 [18], or Ta_2O_5 [19,20,21] are suggested to refer to the literature.

Although titanium dioxide was excluded in Harrop's lists of the dielectrics showing potential application in the MIS structure, the interest centered around this material has been strong. Harbison and Taylor [13] presented their results of hydrolytically deposited TiO_2 films on silicon in 1968. A dielectric constant varying from 50 to 80, and a breakdown strength of 5×10^5 v/cm were reported. It is fairly plausible to attribute such a low breakdown field to the fact that the films deposited were polycrystalline, as pointed out by the authors. Also, capacitance-voltage data indicated a surface state density of approximately 10^{12} states/cm^2-eV, and the Poole-Frenkel effect was considered as the dominant conduction mechanism, as indicated by I-V measurements.

Stoichiometrically, TiO_2 exists in three distinct polymorphic forms: rutile, anatase, and brookite. Both rutile and anatase have the tetragonal structure, whereas brookite shows the orthorhombic structure [9].

Low temperature hydrolytically deposited TiO_2 films were reported by Fitzbibbons, et al. [22]. The as-grown films are amorphous, but annealing in air caused crystallization, with anatase formed beginning at 350°C and rutile at 700°C. The density and index of refraction increased

substantially with increasing annealing temperature, while the etch susceptibility in hydrofluoric acid (HF) and sulfuric acid (H_2SO_4) decreased. Also, an optical band gap of 3.9 eV was obtained. No details on the electrical properties of the films were given.

Electron-beam deposited TiO_2 films were investigated by Brown [9]. Again, the leakage current through the as-deposited films was large. Post deposition oxidation was shown to reduce the magnitude of leakage current. More important is the fact that deposition of TiO_2 films in an oxygen ambient yields a much lower value of leakage current. A surface state density as low as 10^{11} states/cm^2-eV was measured by the quasi-static capacitance-voltage method. Dielectric constants varying from 4 to 40 and optical band gaps of 3.95 eV were also given. Some analysis techniques were used to indicate that thin film TiO_2 is impervious to sodium ion (Na^+) migration, and can be etched in a buffered oxide etch.

Recently, Geraghty, et al. [23] published their results of reactively sputtered TiO_2 films. The as-deposited films are amorphous and can be etched rapidly in HNO_3. The optical absorption spectrum showed an absorption edge at about 330 nm, which corresponds to a band-gap of 3.76 eV. Electrical properties of the as-grown films were not reported.

1.3 Dielectric Films on GaAs

In the 1960's, the III-V compounds attracted considerable attention, and of these materials gallium-arsenide (GaAs) received the most serious consideration. The need for forming insulators with good dielectric and interface properties on GaAs is evident in view of applications to surface passivation and device fabrication. Such a technology will cover a whole range of applications including optoelectronic devices, microwave

field-effect-transitors (FET), and high performance charge-couple-devices (CCD). The dielectric films on GaAs investigated so far have included SiO, SiO_2 [4,5,24], Si_3N_4 [25,26], Al_2O_3 [27], SiO_2-Al_2O_3 [27], Ge_3N_4 [28], and native oxides prepared by thermal oxidation [29], chemical anodization [30, 31], and plasma oxidation [8]. Each of the dielectric films mentioned here will be surveyed in this section with special emphasis on the interface properties.

The properties of the SiO_2-GaAs interface were examined for the first time by Becke, et al [4] in 1965, in an attempt to make a GaAs-FET with SiO_2 as the gate insulator. Room temperature hysteresis and a surface state density of the order of 10^{12} states/cm^2-eV were reported. In 1968, Sato [24] investigated evaporated SiO and pryolytically deposited SiO_2 on GaAs. The instabilities existing in these interface systems were attributed to positive ions in the insulator. Surface state densities in the range of $3x10^{11}/cm^2$-eV were reported. The interface properties of the SiO_2-GaAs interface were further investigated by Kern and White [5] in 1970. The SiO_2 films were deposited primarily by pryolysis of tetraethyl siloxane in argon. Generally, minimum heat exposure (low temperature and short heating period) tended to decrease the interface state density. By combining the optimum conditions (indicated in their papers), a decrease of the interface state density was achieved from values of greater than 10^{13} to $10^{11}/cm^2$-eV.

The electrical properties of the Si_3N_4-GaAs interface determined by C-V characteristic was scrutinized by Foster [25] in 1970. The Si_3N_4 films were pyrolytically deposited from silane (SiH_4) and ammonia (NH_3) in the range 650-750°C on n- and p- type, (111) GaAs. The C-V curves obtained on p- and n- substrates showed the presence of fast surface states and room temperature hysteresis. By increasing the frequency of

the a-c signal in the C-V measurement to freeze out the fast surface states. the difference in the frequency response of the fast surface states associated with the films deposited at different NH_3 to SiH_4 ratios was observed. Room temperature bias stress showed that the instabilities were due to charge injection and subsequent trapping in the insulator. Flat band voltages were reported to be about -15 V and +20 V for p- and n- substrates, respectively. Moreover, n-type samples showed much poorer repeatability from run to run than did p-type samples. Surface state densities in the 10^{12} - $10^{13}/cm^2eV$ range were also obtained by comparing a high frequency C-V curve with a theoretical one calculated for the same insulator thickness and substrate doping [32]. The Si_3N_4-GaAs interface in depletion region were further investigated by Cooper, et al. [26] in 1972, using the conductance-voltage (C-V) technique. A significant density of traps was observed in the bulk insulator. It was proposed that the density of trap states was a function of both energy and distance from the interface. It was also concluded that in the first few angstroms of the insulator the states associated with the interface added to the insulator traps so that the net density of states became greater than in the bulk insulator.

An inversion mode GaAs-MISFET was realized by Ito and Sakai [33] using the alloying technique for formation of source and drain contacts, and chemical-vapor-deposited double layer films of Al_2O_3 and SiO_2 as gate insulators. No hysteresis phenomenon due to interface states or bulk traps was recognized in their studies. This result seems fairly acceptable if it is considered that the main instabilities in SiO_2 and Al_2O_3 are due to ion migration and traps, respectively.

The electrical properties of the Al_2O_3-, Si_3N_4-, and SiO_2-GaAs interfaces were restudied by Miyazaki [6] in 1974. The energy distribution of the interface state density was obtained from the high frequency C-V curves. All samples exhibited an U-shaped distribution with the largest values located between mid-gap and Fermi level. The values depended on the substrate conductivity type and the deposition conditions of the insulator films, and ranged from 0.9×10^{11} to $20 \times 10^{11}/cm^2$-eV for p-type substrates and from 1×10^{12} to $4 \times 10^{12}/cm^2$ eV for n-type substrates. It was indicated that the interface state densities were higher for Si_3N_4 films than for other insulating films. Frequency dispersion in the accumulation region on n-type substrates was also observed. This was considered to be due to deep traps formed by oxygen-atom doping during oxide deposition.

Recently, much interest has centered around the anodic native oxide of GaAs due to the fact that this is a room temperature process, and surface state densities can be drastically reduced after an appropriate low temperature annealing. Anodic oxidation of GaAs was first reported by Revesz and Zaininger [34] in 1963 but resulted in a severely pitted surface. Growth of uniform films with low conductivity was first reported in 1973 [30] using a constant voltage anodization in an aqueous solution of H_2O_2. Recently, Hasegawa, et al. [31] reported a new method of growing anodic native oxides of GaAs with good dielectric and interface properties. A breakdown field strength of 5×10^6 V/cm and a relative dielectric constant, measured at 1 MHz, of 7-8 were reported. Fairly large hysteresis was shown for the as-grown oxide, which gave an effective flat-band voltage shift (ΔV_{FB}) of about 15V. More important is the fact that short time, low temperature (300°C) annealing in hydrogen results in greatly improved

interface properties with a density of fast interface states near midgap of $2 \times 10^{11}/cm^2 eV$.

Plasma oxidation of GaAs was recently reported by Chang and Sinha [8]. The current-voltage characteristic at room temperature showed that the d-c conduction was mainly a bulk-limited Frenkel-Poole [35] mechanism. The absence of a well-defined inversion region in the as-grown oxide was attributed to either high surface state densities or high leakage current through the oxide. Instabilities predominantly due to slow trapping were also reported.

More recently, Bagratishvili, et al. [28] reported their results of the Ge_3N_4-GaAs interface properties. A dielectric constant of 6.5, breakdown field strength of 3×10^6-6×10^6 V/cm, and an optical gap of 4.4 eV were reported. It is important to note that the interface properties of the structure were observed to become poorer upon raising the annealing temperature. Hysteresis was also attributed to trapping effects.

In summary, the general features associated with the C-V characteristics of GaAs-MIS structures are (1) room temperature hysteresis caused by trapping effect (except SiO_2), (2) high surface state densities (10^{11}-$10^{13}/cm^2 eV$), (3) difficulty in obtaining an inversion layer without a suitable heat treatment, and (4) large frequency dispersion in the accumulation region. The author believes that at the present stage, except for the TiO_2 films studied here, only the native oxide and germanium nitride deserve further investigation to achieve the level of practical application.

2. THEORETICAL BACKGROUND

Certain fundamental theories which are crucial in understanding the present study will be discussed in this chapter. D-C conduction is generally employed to check the quality of the insulators as well as to identify the pertinent conduction processes. The capacitance-voltage characteristic of an MIS capacitor is believed to be a versatile technique in studying the properties of insulator-semiconductor interfaces. The study of localized states in the forbidden gap of a non-crystalline solid is also very interesting. Optical absorption is one of the techniques used in this study. The relation between these two will be discussed.

2.1 Current-Voltage Characteristics

Among the many techniques for studying the properties of dielectric films, d-c conduction has attracted less interest than it may deserve. The reason for this may be found in the fact that most researchers wish their dielectric films to be good insulators and therefore consider conduction through the films as a nuisance. Although comprehensive reviews in this field have been available [36,38], controversies still remain in certain areas, such as the separation of the ionic and electronic conduction and even the basic problem of whether the conduction is electrode-limited and/or bulk-limited [39].

Ideally, the insulating film of an MIS or (MIM) structure should exhibit zero conductance. In practice however, typical insulators may show conduction at considerably lower fields than those required for the intrinsic processes in the ideal insulator. This conduction may be linear or non-linear, and may be due to electronic and/or ionic conduction. The number of free electrons in the conduction band of a large band-gap insulator in

thermal equilibrium is negligible in most practical cases. Conduction can take place only after carriers have been introduced into the conduction band of the insulator by various mechanisms. Some of these mechanisms are: injection of electrons from a contact over a barrier, tunneling through a barrier from a contact, and electron emission from traps. The tunneling process is inherent to very thin films, and accordingly will not be considered here. Injection of electrons from a contact over a barrier is called Schottky emission [40], whereas electron emission from the traps is called Poole-Frenkel emission [35]. The former is an electrode-limited process, while the latter is a bulk-limited one. Most of the insulators investigated for application in MIS devices exhibit d-c conduction either due to Schottky emission [41] or due to Poole-Frenkel emission [39,42,43]. Only these two processes will be considered in detail in this section.

The equation, called the Richardson thermionic emission equation, describing the emission of electrons from a metal surface into the vacuum is

$$J = \frac{4\pi mek^2T^2}{h^3} \exp\left(-\frac{\phi}{kT}\right)$$

$$= AT^2 \exp\left(-\frac{\phi}{kT}\right) \qquad (2.1)$$

where J is the current density, m is the mass of electron, e is the magnitude of electron charge, ϕ is the metal work function, k is Boltzmann's constant, h is Planck's constant, and T is the absolute temperature. Certain modifications have to be considered as one applies the Richardson thermionic emission equation to the case of a metal-insulator interface. It is well understood that a positive charge will

be induced on the metal surface as an electron is placed at a distance x from the metal surface. The attractive force between the electron and the induced positive charge is called the image force. The potential energy of the electron due to this image force is given by

$$\phi_{im} = \frac{e^2}{16\pi\varepsilon_o K^* x} \tag{2.2}$$

The dielectric constant K* is the high-frequency constant, since in the course of emission from the electrode the transit time of escaping electrons is short compared to the dielectric relaxation time [2]. The potential barrier with the attendant image potential as a function of x, and in the presence of an electron, is givey by

$$\phi(x) = \phi_o + \phi_{im} = \phi_o - \frac{e^2}{16\pi\varepsilon_o K^* x} \tag{2.3}$$

In the presence of a uniform electrip field, -E, the expression is then given by

$$\phi(x) = \phi_o - \frac{e_2}{16\pi\varepsilon_o K^* x} - e\,E\,x \tag{2.4}$$

where ϕ_o is the ideal interfacial barrier height. This equation has a maximum at $x_m = (e/16\pi K^*\varepsilon_o E)^{1/2}$. The barrier lowering due to the interaction of the applied field with the image potential is given by

$$\begin{aligned}\Delta\phi_s &= \phi_o - \phi(x_m) \\ &= \left(\frac{\varepsilon^3}{4\pi K^*\varepsilon_o}\right)^{1/2} E^{1/2} \\ &= \beta_s E^{1/2}\end{aligned} \tag{2.5}$$

where

$$\beta_s = \left(\frac{e^3}{4\pi K^* \varepsilon_o}\right)^{1/2}$$

Substituting $\phi_o - \Delta\phi_s$ for ϕ in Equation (2.1), one obtains

$$J = AT^2 \exp\left(-\frac{\phi_o}{kT}\right) \exp\left(\frac{\beta_s E^{1/2}}{kT}\right) \qquad (2.6)$$

which is called the Schottky emission equation. Thus, the attenuation of a metal-insulator barrier arising from the electrode image force interaction with the field at the metal-insulator interface is called the Schottky effect. Figure 2.1 shows the schematic illustration of the Schottky effect.

A process called Poole-Frenkel emission, which is a bulk analogue to the Schottky emission at the interfacial barrier, will be discussed in the remainder of this section. The Poole-Frenkel effect, or field-assisted thermal ionization, is the lowering of a Coulombic potential barrier when it interacts with an electric field as shown in Figure 2.2. Consider the case of a donor site in which an electron is trapped. The potential energy of the electron is $-e^2/4\pi K^* \varepsilon_o x$, where K^* is the optical dielectric constant, and x is the distance from the positive ion. In the presence of the electric field, the potential energy of the electron becomes

$$\Delta\phi(x) = -\frac{e^2}{4\pi\varepsilon_o K^* x} - e\,E\,x \qquad (2.7)$$

The barrier lowering, denoted as $\Delta\phi_{PF}$, is the maximum value of $|\Delta\phi(x)|$. After some manipulations similar to the case of Schottky emission, one gets

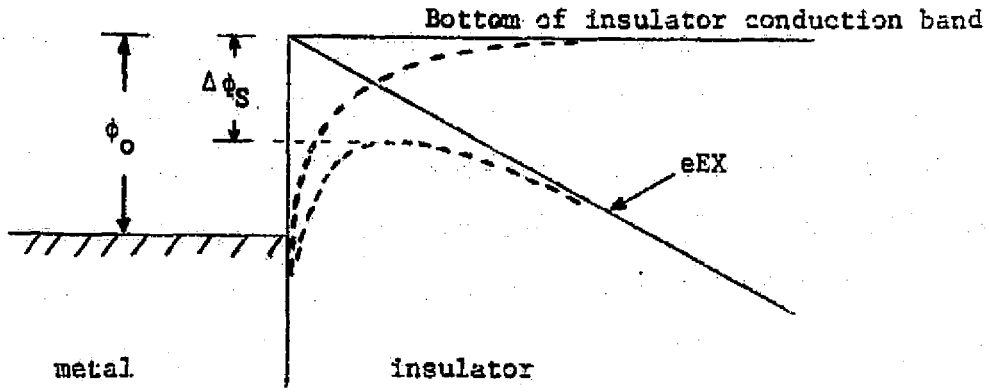

Figure 2.1. Schematic illustration of Schottky effect

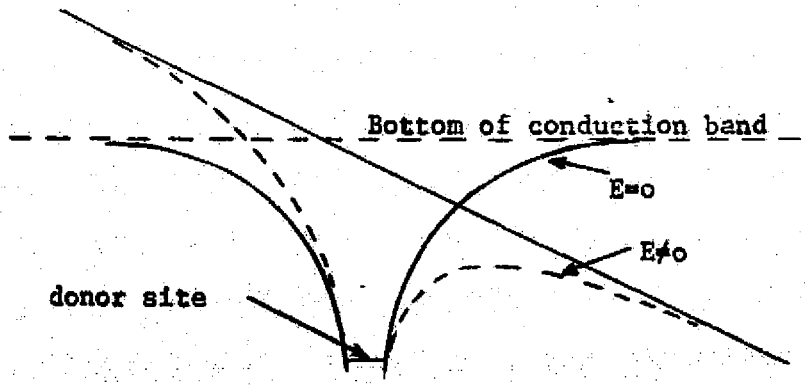

Figure 2.2 Schematic representation of Poole-Frenkel emission

$$\Delta\phi_{PF} = \left(\frac{e^3}{\pi\varepsilon_o K^*}\right)^{1/2} E^{1/2}$$

$$\equiv \beta_{PF} E^{1/2} \qquad (2.8)$$

where $\beta_{PF} = \left(\frac{e^3}{\pi\varepsilon_o k^*}\right)^{1/2}$. This result was first applied by Frenkel [35] to the host atoms in bulk semiconductors and insulators. He proposed that the ionization energy of the atoms in a solid is lowered an amount given by Equation (2.8) in the presence of the electric field. The fact that the illumination of a semiconductor can result in an increase in conductivity independent of E supports the contention that the increase in electrical conductivity in an intensive field is due to the increase of the number of free electrons rather than that of the mobility. Therefore, discussion will be centered around the dependent of the free carrier concentration on the electric field. The electron concentration of an intrinsic material is

$$n = (N_C N_V)^{1/2} \exp[-(E_C - E_V)/2kT] \qquad (2.9)$$

where N_C is the effective density of states in the conduction band, N_V is the effective density of states in the valance band, and E_C and E_V have their usual meanings. For an n-type material with no acceptor sites [44]

$$n = (N_C N_D/2)^{1/2} \exp[-(E_C - E_d)/2kT] \qquad (2.10)$$

where N_D is the density of donor sites and E_d is their energy level. A similar expression applies to p-type materials with no donor sites. Equations (2.9) and (2.10) are of the form

$$n = n_c \exp(-\phi/2kT) \qquad (2.11)$$

where ϕ is the energy difference between the emission site and the bottom of the conduction band. After substituting the Poole-Frenkel effect of barrier lowering as described by Equation (2.8) into Equation (2.11), one obtains

$$n \propto \exp(\beta_{PF} E^{1/2}/2kT) \qquad (2.12)$$

Thus the conductivity is field-dependent and of the form

$$\sigma = \sigma_o \exp(\beta_{PF} E^{1/2}/2kT) \qquad (2.13)$$

where σ_o is the low-field conductivity. Equation (2.13) may be written in the form

$$J = J_o \exp(\beta_{PF} E^{1/2}/2kT) \qquad (2.14)$$

where $J_o = \sigma_o E$ is the low-field current density.

When trap and acceptor sites are present, the situation may be different. Since these levels are lower in energy than the bottom of the conduction band, they tend to fill first. When the number of the electrons in the conduction band is small compared to either donor or acceptor density, i.e., $n \ll N_D$, $n \ll N_A$, then the concentration of electrons is given by [44]

$$n = [N_C (N_D - N_A)/2N_D] \exp[-(E_C - E_D)/kT]$$

$$= n_o \exp(-\phi/kT) \qquad (2.15)$$

Therefore, the current density for the Poole-Frenkel effect with compensation present is given by

$$J = J_o \exp (\beta_{PF} E^{1/2}/kT) \qquad (2.16)$$

In general, the Poole-Frenkel effect is governed by an equation of the form [45]

$$J_{PF} = J_o \exp (\beta_{PF} E^{1/2}/rkT) \qquad (2.17)$$

where r describes the degree of compensation.

After scrutinizing Equations (2.6) and (2.17), one concludes that both Schottky emission and Poole-Frenkel emission can be generally described by an equation of the form

$$J = J_o \exp (\beta E^{1/2}/kT) \qquad (2.18)$$

Therefore, whether a conduction process is Schottky emission (electrode-limited) or Poole-Frenkel emission (bulk-limited) can be determined by measuring the slope of log(I) vs. $E^{1/2}$ plot.

2.2 Capacitance-Voltage Characteristics of MIS Capacitors

The experimental technique utilizing an MIS capacitor to investigate the properties of the insulator-semiconductor interface involves measuring either the resistive component (G-V) or reactive component (C-V) of the MIS impedance. Among the various applications of the C-V characteristic, the measurement of the fast surface state density is one of the most widely used. Before going into the discussion of the C-V characteristic, the present state of the knowledge about the surface state measurement will

be briefly reviewed. In general, the most commonly used techniques [46] are the high frequency C-V described by Terman [32,47,48], the low frequency or quasi-static technique suggested by Berglund [49] and Kuhn [50], and a-c conductance technique by Nicollian and Goetzberger [51]. The relative advantages and disadvantages of these techniques have been compared in detail by Declerck, et al. [52]. The conductance-voltage (G-V) technique by Nicollian-Goetzberger is believed to be the most complete and accurate one at the present time. A surface state density as low as 10^{9} cm^{-2} eV^{-1} has been measured by virtue of this technique [52]. In addition, not only the surface state density but also the electron (or hole) capture cross-section can be obtained by directly fitting the experimental curve to the theoretical one. However, a large number of measurements are required to achieve such detailed results, and only that portion of the energy gap between mid-gap and the Fermi-level can be examined with this technique [50]. The original low frequency C-V technique of Berglund has the advantage of covering a wider range in the gap. However, researchers have reported that sometimes this is also hard to achieve due to the limitation of the experimental technique. The low frequency C-V curve is easy to obtain by using the quasi-static technique of Kuhn. A sensitivity of the order of 10^{10} cm^{-2} eV^{-1} for this quasi-static low frequency technique has been reported [52]. The high frequency capacitance technique developed by Terman yields surface state densities by the comparison of a high frequency C-V curve with an ideal one. The limitations of this technique have also been studied [53], and the most serious limitation is that a graphical differentiation of the analyzed data is required. Therefore, measurement of surface state densities as low as 10^{10} cm^{-2} eV^{-1} with this technique generally cannot

be achieved [52]. In spite of the disadvantage for the high frequency C-V technique described here, it will be employed in this study due to its simplicity and its convenience in analyzing the instabilities associated with the MIS capacitor. Moreover, the surface state density associated with the TiO_2-GaAs interface is expected to be much higher than the limiting sensitivity of this technique.

The detailed treatment of the C-V characteristic can be found elsewhere [2,11]. Only the materials that deals with the frequency dependence of the C-V curve and the density-of-surface state calculations will be presented here.

Consider an MIS capacitor as shown in Figure 2.3. In analyzing a capacitor it is convenient to start from the consideration of charge storage. For convenience, all the various kinds of charge considered here are referred to charge per unit area. When a voltage V_G is applied to the MIS capacitor, the charge at the metal plate Q_M is balanced by the charge in the semiconductor, Q_T, either in surface states, Q_{SS}, or in the semiconductor space charge region, Q_{SC}.

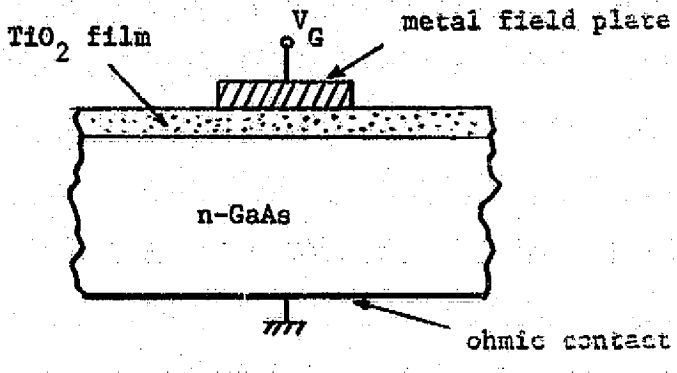

Figure 2.3. Schematic representation of the metal-TiO_2-GaAs MIS capacitor

Thus,

$$Q_M = - Q_T = - Q_{SS} - Q_{SC} \tag{2.19}$$

In the absence of a work-function difference between the metal and semiconductor, the applied gate voltage will appear partly across the oxide and partly across the semiconductor. Thus,

$$V_G = V_o + V_S \tag{2.20}$$

where V_o and V_S denote the potential variation across the oxide and semiconductor, respectively. The total capacitance of the MIS capacitor is given by

$$C = \frac{dQ_M}{dV_G} \tag{2.21}$$

Substituting Equations (2.19) and (2.20) into (2.21), one obtains

$$\frac{1}{C} = \frac{1}{C_o} + \frac{1}{C_S} \tag{2.22}$$

where $C_o = \frac{dQ_M}{dV_o}$ is the insulator capacitance and $C_S = - \frac{dQ_T}{dV_S}$ is the semiconductor capacitance. If the relation $Q_T = Q_{SS} + Q_{SC}$ is employed, C_S can then be written as

$$C_S = C_{SS} + C_{SC} \tag{2.23}$$

where $C_{SS} = - \frac{dQ_{SS}}{dV_S}$ is the surface state capacitance and $C_{SC} = - \frac{dQ_{SC}}{dV_S}$ is the semiconductor space-charge capacitance. According to Equations (2.22) and (2.23), the total capacitance of the MIS capacitor is given by

$$\frac{1}{C} = \frac{1}{C_o} + \frac{1}{C_{SS}+C_{SC}} \qquad (2.24)$$

Equation (2.24) indicates that an MIS capacitor can be considered as an insulator capacitor in series with a parallel combination of two capacitors, associated with charge storage in the space-charge region and in surface states, respectively. As a matter of fact, this representation is valid only when the various loss mechanisms are neglected. A fairly complete equivalent circuit of the MIS capacitor including all the loss mechanisms is shown in Figure 2.4 if the capacitor is biased in the depletion or inversion region [54]. The current flow in the MIS structure can be understood in terms of three parallel current paths: (1) a path through C_D, the depletion layer space-charge capacitance; (2) a path through R_{nD}, R_{nS}, and C_{SS}, representing the resistance associated with the electron flow across the depletion region, the loss mechanism due to the trapping of electrons by surface states, and the capacitance due to changes in the surface state charges as a result of electron trapping, respectively; (3) a path through R_{PB}, R_{PD}, R_{PS}, and C_{SS}, representing the resistance due to the diffusion of holes in the neutral region, the resistance due to the diffusion of holes across the depletion region, the loss mechanism due to the trapping of holes by surface states, and the capacitance associated with changes in the surface state charges as a result of hole trapping, respectively. The capacitance C_I represents the minority carrier storage in the inversion layer at the insulator-semiconductor interface. C_o is the oxide capacitance, and R_o is the bulk resistance. This equivalent circuit has been further simplified and modified by Saka [46] as shown in Figure 2.5. Note that R_g is included to account for the generation-recombination mechanism.

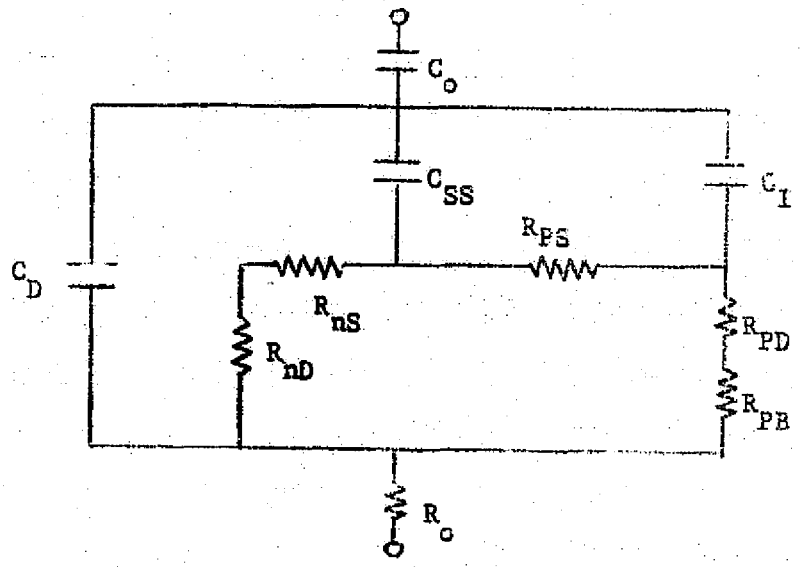

Figure 2.4. Equivalent circuit of an MIS capacitor

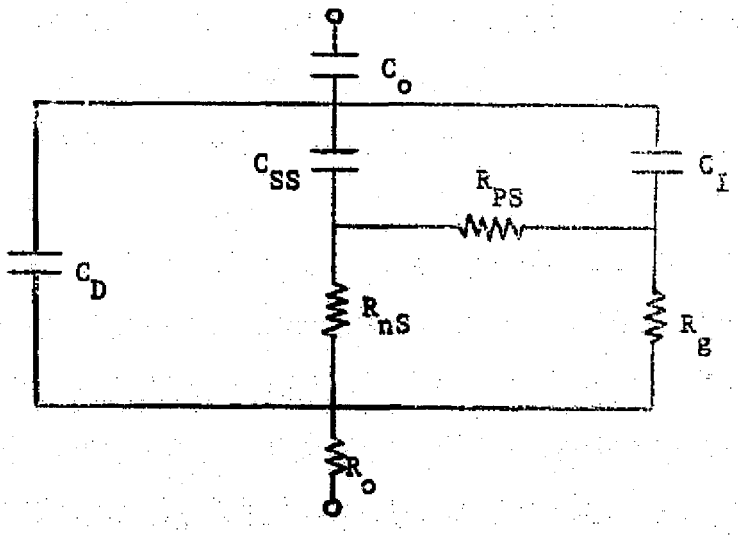

Figure 2.5. Simplified equivalent circuit of an MIS capacitor

When a voltage is applied to an MIS capacitor, there are basically three types of bias conditions, which are accumulation, depletion, and inversion. Each of these is associated with a specific range of semiconductor surface potential [2]. If it is assumed that all the charge in the oxide is near the semiconductor-insulator interface, the electric field within the oxide is uniform. Then from Gauss' law it can be shown that

$$C = \frac{dQ_M}{dV_G} = \frac{d(C_o V_o)}{dV_G}$$

$$= C_o \left(1 - \frac{\partial V_S}{\partial V_G}\right) \qquad (2.25)$$

If the voltage equivalents of the charge in surface state, V_{SS}, and the charge in the space charge layer, V_{SC}, are defined as $V_{SS} = \frac{Q_{SS}}{C_o}$ and $V_{SC} = \frac{Q_{SC}}{C_o}$, Equation (2.20) can be written as

$$V_G = V_{SS} + V_{SC} + V_S \qquad (2.26)$$

Therefore,

$$\frac{\partial V_S}{\partial V_G} = \frac{1}{1 + \frac{\partial V_{SC}}{\partial V_S} + \frac{\partial V_{SS}}{\partial V_S}} \qquad (2.27)$$

The MIS capacitance as a function of surface potential is obtained after substituting Equation (2.27) into (2.25), i.e.,

$$C(V_S) = C_o \frac{(\partial V_{SC}/\partial V_S) + (\partial V_{SS}/\partial V_S)}{1 + (\partial V_{SC}/\partial V_S) + (\partial V_{SS}/\partial V_S)} \qquad (2.28)$$

If the frequency of the a-c signal is so high that none of the surface states can follow, then $\partial V_{SS}/\partial V_S$ approaches zero. If this is the case, the MIS capacitance reduces to

$$C = C_o \frac{\partial V_{SC}/\partial V_S}{1 + (\partial V_{SC}/\partial V_S)} \qquad (2.29)$$

If the bias condition is such that $\partial V_{SC}/\partial V_S \gg 1$, i.e., $C_{SC} \gg C_o$, then $C \to C_o$, which corresponds to the accumulation region in Figure 2.6. In the inversion region, curve (2) holds if the minority carriers cannot achieve equilibrium. If they can follow the applied bias, but not the a-c signal, curve (1) applies. At large negative potentials, the space-charge layer is in the inversion region and the space charge capacitance

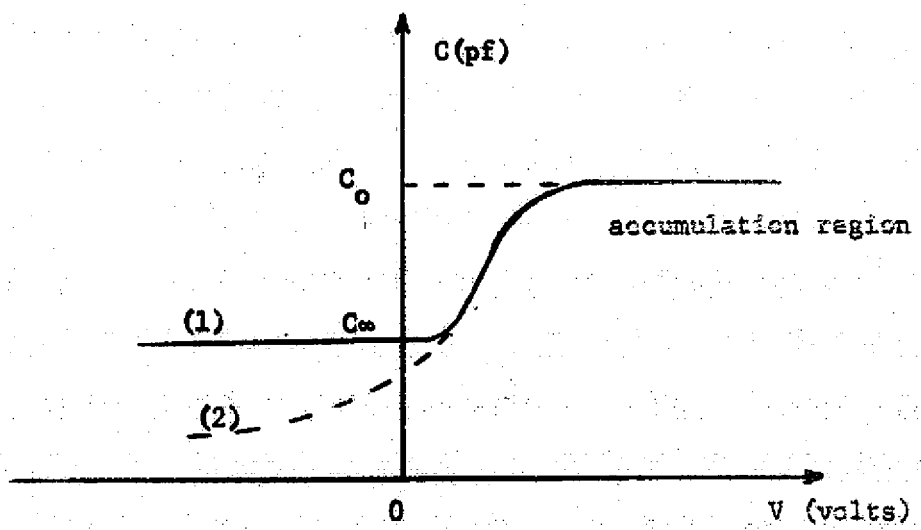

Figure 2.6. High frequency C-V characteristic of the MIS capacitor

arising from majority carriers is given by [54]

$$C_{SC}^{\infty} = \frac{1}{2}\left[\frac{N_D\, q\, \varepsilon\, \varepsilon_o}{(kT/q)\, \ell n(N_D/n_i)}\right]^{1/2} \qquad (2.30)$$

where N_D is the doping level. This C_{SC}^{∞} in series with C_o accounts for the flat portion of the C-V curve, labeled C_∞, where

$$C_\infty = \frac{C_{SC}^{\infty}\, C_o}{C_o + C_{SC}^{\infty}} \qquad (2.31)$$

As far as the flat band voltage and surface state density are concerned, the result of Lehovec [54] will be used. The resulting expression for the flat-band capacitance, C_{FB}, of the observed C-V curve is given by

$$\frac{C_o - C_{FB}}{C_o - C_\infty} = \frac{C_o}{C_o + 2C_\infty\sqrt{\ell n(N/n_i)-1}} \qquad (2.32)$$

The intersect of the flat-band capacitance with the observed C-V curve provides the flat-band voltage. The density of surface states, D, at the flat-band voltage is

$$D = \frac{(C_o - C)C}{3\,\frac{\partial C}{\partial V}\,qkT} - \frac{C_o}{(C_o - C)q^2} \qquad (2.33)$$

The values of C and $\partial C/\partial V$ are to be taken from the experimental C-V curve at the flat-band voltage.

2.3 Band Model and Optical Absorption of Amorphous Solids

The band model is fundamentally important in understanding the electrical and optical properties of materials. It is only since about 1960 that the theory of electrons in non-crystalline materials has become an important part of solid state physics [55]. It is well-known that in crystalline materials both a conduction band and a valance band are well defined and sharply separated by a forbidden gap, which is linked with the behavior of electrons in the periodic crystal potential. The situation for amorphous materials is completely different due to the lack of long range order. Therefore, the potential in which the electrons move is no longer periodic. Nevertheless, it is generally accepted that there exists a band gap in the density of states of the amorphous materials as manifested by the transparency of the glasses known to everyone. Some of the questions concerning the effects of disorder on the electronic states of an amorphous material are still open to debate, and controversies still remain as whether or not there exist localized states in the gap [12]. It is the purpose of this section to introduce a somewhat generally accepted band model, called the Mott-CFO model [56,57], and then discuss the optical absorption.

The Mott-CFO band model, proposed by Mott in 1967 and Cohen, Fritzsche, and Ovshinsky in 1969, is shown in Figure 2.7. The shaded area represents the localized states. The optical gap is defined by $E_g^{opt} = E_c - E_v$, where E_c and E_v are obtained experimentally by extrapolating the densities corresponding to the extended states. The important feature of this model is contained in the two energies, E_c and E_v, which separate the localized tail states from the band (or extended) states. This arises from the fact

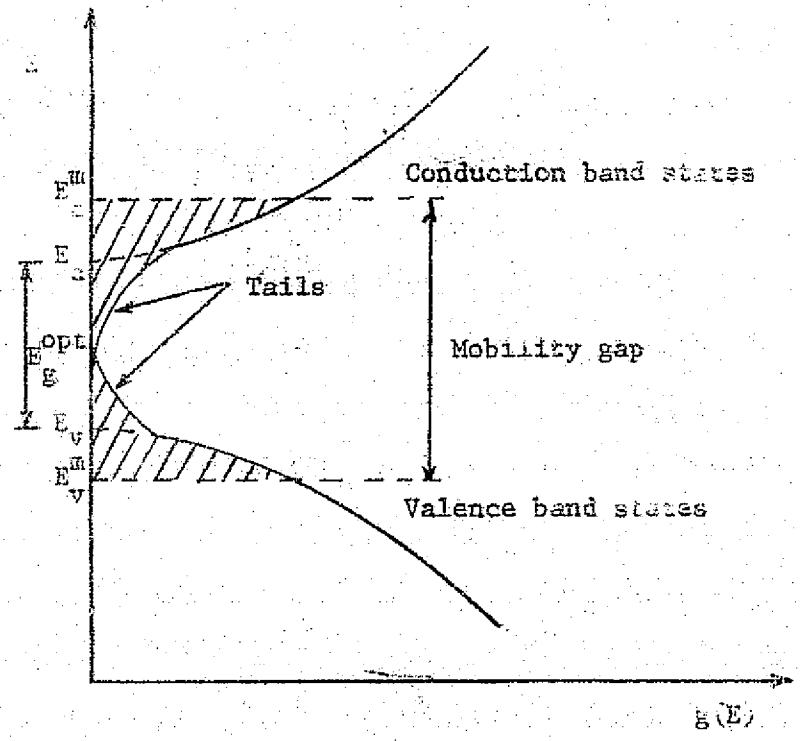

Figure 2.7. Density of states of the amorphous solid in the Mott-CFO model.

that the large difference in the conductivities of amorphous and crystalline semiconductors cannot be explained by the scattering of a quasi-free carrier on the disordered lattice. Therefore, it is necessary to conclude that the disorder changes the character of the wave functions, the states become localized and the conduction mechanism changes. Although the density of states is assumed to decay exponentially into the forbidden gap, the states in the exponential tail are localized and hence make little contribution to electron transport processes. This feature is manisfested in Figure 2.8 as proposed by Cohen, et al. [57].

Amorphous semiconductors or insulators are transparent in the infrared region. The onset of optical interband transitions defines an energy gap between the valence band and conduction band. Figure 2.9

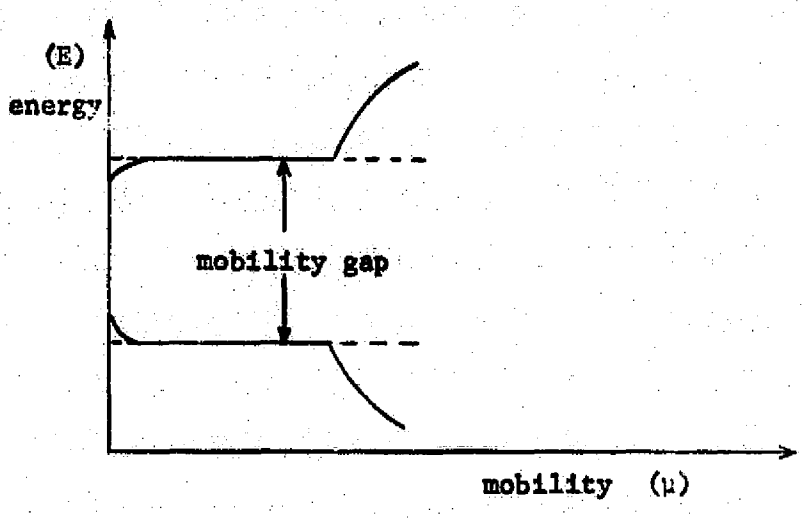

Figure 2.8. Mobility as a function of energy in an amorphous semiconductor

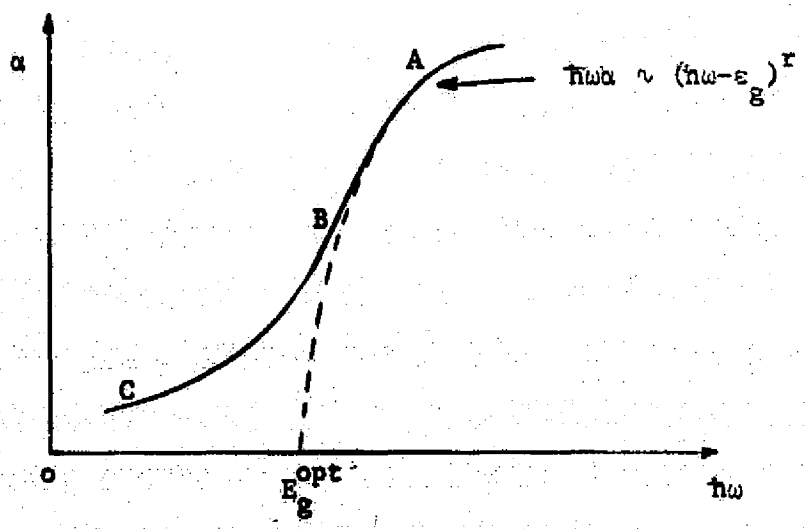

Figure 2.9. Absorption coefficient α versus photon energy ħω for α - As_2S_3, after Tauc [58]

shows the optical absorption of $\alpha - As_2S_3$ given by Tauc and Menth [58]. In view of the high optical absorption coefficient, part A is apparently due to transitions associated with the states close to the mobility edges. A common, but not universal, behavior of the absorption coefficient in this energy range is

$$\alpha = \text{constant } (\hbar\omega - \varepsilon_o)^2/\hbar\omega \qquad (2.34)$$

where α is the absorption coefficient and $\hbar\omega$ is the photon energy. The gap, ε_o, can be defined by using this equation. Derivations leading to this result will be shown below. Certain concepts paralleling those of crystalline solids are borrowed except that the momentum-conservation selection rule is relaxed due to the fact that the momentum is no longer a meaningful quantum number for amorphous semiconductors.

The relation between the absorption coefficient α and the transition probability P is governed by

$$\alpha = \frac{\hbar\omega P}{|\vec{S}|} \qquad (2.35)$$

where $\vec{S}$, is the Poynting vector of the incident radiation. The transition probability P is given by

$$P \propto \frac{1}{\hbar\omega} \int_o^\infty \int_o^\infty g_c(\varepsilon_c') \, g_v(\varepsilon_v') \, \delta \, (\varepsilon_c' + \varepsilon_v' - \varepsilon_m) \, d\varepsilon_c' \, d\varepsilon_v' \qquad (2.36)$$

under the assumption that the matrix element H associated with the transitions is independent of the photon energy [1]. Here

$$\begin{aligned} \varepsilon_c' &= E - E_c \\ \varepsilon_v' &= E_v - E \\ \varepsilon_m &= \hbar\omega - \varepsilon_o \end{aligned} \qquad (2.37)$$

Note that the incorporation of the δ-function guarantees energy conservation. After integrating the δ-function, we get

$$P \propto \frac{1}{\hbar\omega} \int_0^{\infty} g_v(\varepsilon_v')\, g_c(\varepsilon_m - \varepsilon_v')\, d\varepsilon_v' \qquad (2.38)$$

If the sharp termination of the density of states is true, i.e., $g_c(\varepsilon_m - \varepsilon_v') = 0$ if $\varepsilon_m < \varepsilon_v'$, then

$$P \propto \frac{1}{\hbar\omega} \int^{\varepsilon_m} g_v(\varepsilon_v')\, g_c(\varepsilon_m - \varepsilon_v')\, d\varepsilon_v' \qquad (2.39)$$

If we assume $g_v \propto (E_v - E)^S = \varepsilon_v'^S$ and $g_c \propto (E - E_c)^P = \varepsilon_c'^P$ and integrate by changing variables, we obtain

$$P \propto \frac{\varepsilon_m^{S+P+1}}{\hbar\omega} \left[\int_0^1 (1-y)^P\, y^S\, dy\right] \qquad (2.40)$$

The quantity in the bracket is known to be $\Gamma(S + 1)\, \Gamma(P + 1)/\Gamma(S + P + 1)$, where $\Gamma(S)$ is the gamma function. Combining Equations (2.35), (2.37), and (2.40), we finally obtain

$$\alpha \propto \frac{(\hbar\omega - \varepsilon_o)^{S+P+1}}{\hbar\omega} \qquad (2.41)$$

Equation (2.34) is readily obtained if we assume $S = P = \frac{1}{2}$, i.e., both the extended bands have parabolic densities of states.

Finally the absorption coefficients associated with band-to-band transitions for crystalline or polycrystalline materials are simply listed as follows, and are discussed in detail elsewhere [1].

$$\alpha \propto (\hbar\omega - \varepsilon_g)^{1/2} \quad \text{for a direct band gap material.} \qquad (2.42)$$

$$\alpha \propto (\hbar\omega - \varepsilon_g \pm \hbar\omega_p)^2 \quad \text{for an indirect band gap material.} \qquad (2.43)$$

where ε_g is the energy of the band gap, and $\hbar\omega_p$ is the phonon energy. Plotting α vs. $\hbar\omega$ is one of the commonly used techniques to idenfity whether a material has a direct-band gap or indirect-band gap.

3. EXPERIMENTAL TECHNIQUES

In this chapter, the procedure for fabrication of the devices used in this study is described. X-ray diffraction to determine the film structure, ellipsometry to measure film thickness and refractive index, and optical absorption are then discussed. A substantial effort in this research is applied to the study of the current-voltage (I-V) and capacitance-voltage (C-V) characteristics, from which the properties of the insulator and those of the insulator-semiconductor interfaces are determined.

3.1 Chemical Vapor Deposition of Titanium Dioxide Films

Chemical vapor deposition (CVD) is one of the most widely used techniques for the preparation of thin films for solid state devices, as well as films for optical and protective coatings. Chemical vapor deposition offers several advantages in the film growth. These are: versatility in choice of the substrate, uniformity and reproducibility of the films, the achievement of homogeneous composition, easy control over the thickness and growth rate, and ease in varying the substrate temperature to meet special purposes [59]. A detailed description of the CVD process for the preparation of TiO_2 was given by Harbison and Taylor [13]. Both the hydrolysis and pyrolysis of organometallic compounds were mentioned. Water vapor used in hydrolysis is generated by the reaction $H_2 + CO_2 \rightarrow H_2O + CO$ at the substrate if the temperature of the gases is greater than 800°C. It is readily apparent that this kind of high temperature process is particularly undesirable if the substrate is a III-V compound. Consequently, the low temperature pyrolysis process is used in this study

Tetraisopropyl titanate (TPT), Ti $(OC_3H_7)_4$, obtained from the Ventron Corporation was used in this study due to its high vapor pressure at room temperature. The suggested reaction is as follows:

$$Ti(OC_3H_7)_4 \xrightarrow{\Delta} TiO_2 + \text{volatile exhaust.}$$

Figure 3.1 illustrates the deposition apparatus. The mixing chamber serves as a buffer and helps the TPT and main flow mix homogeneously before entering the reaction chamber. The reaction furnace is R-F induction-heated, which allows the furnance temperature to range from room temperature to 1200°C. The exhaust is connected to an oil bath to prevent oxygen contamination of the reaction chamber. Details on operating this apparatus are presented in the next section.

3.2 Device Fabrication

For the purpose of this study, both the metal-insulator-semiconductor (MIS) and metal-insulator-metal (MIM) structures were fabricated. The fabrication of the MIS devices included the following steps:

i) Preparation of the substrates.

ii) Deposition of TiO_2 thin films.

iii) Annealing of the films, if required.

iv) Metallization.

The procedure for fabricating MIM devices is the same as for MIS devices except before step ii) a thin metal layer is evaporated on an insulating substrate (fused quartz is used here). Each step listed above will now be considered in more detail.

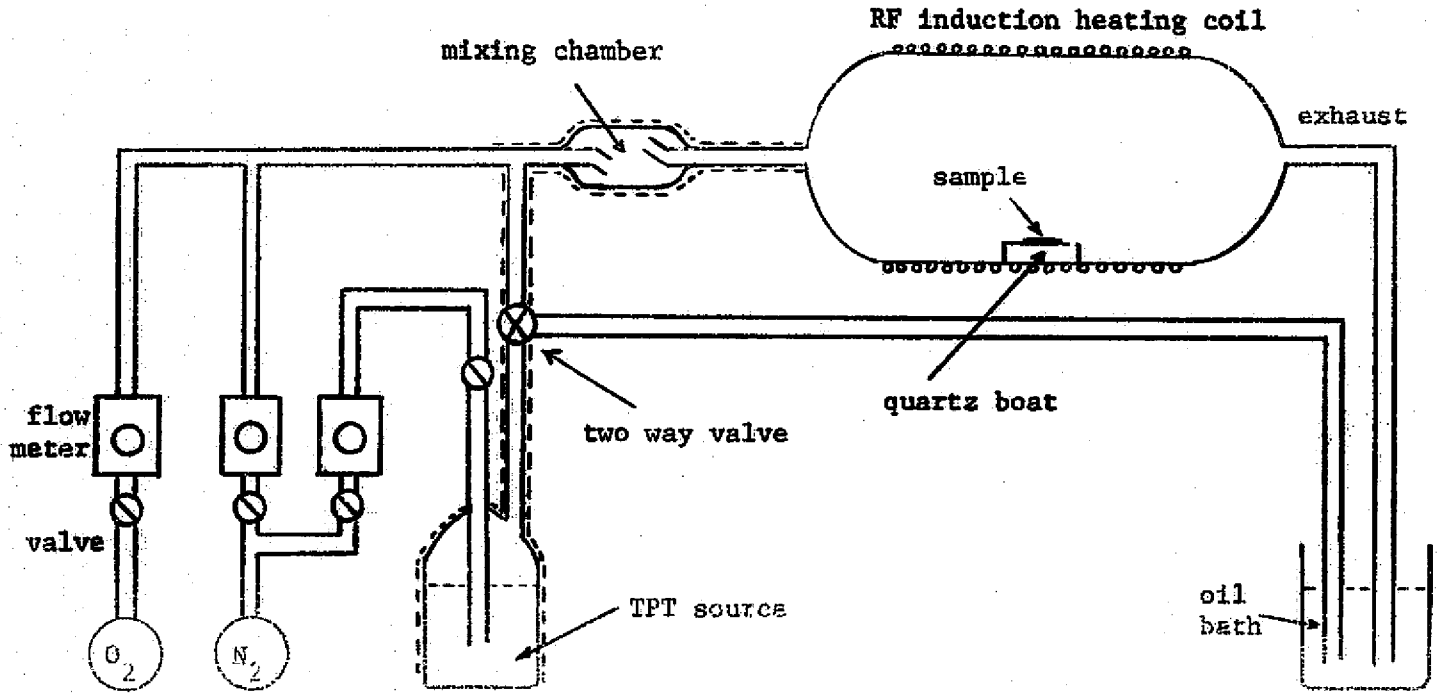

Figure 3.1. Schematic representation of the CVD apparatus

i) Preparation of the substrates

The wafers used in this study are n-type, epitaxial-grown, tellurium (Te)-doped gallium-arsenide provided by Laser Diode Laboratories, Inc. The epi-layer is (100) oriented and has a carrier concentration of 1.2 x 10^{17} cm^{-3}. The thickness of the layer and substrate are 70 microns and 300 microns, respectively. The n^+ substrate has a doping level as high as 10^{18} cm^{-3}. After being cut into pieces of approximately 0.5cm x 0.8cm area, the wafers were cleaned in trichlorethylene (TCE) to remove wax, then acetone to eliminate organic contamination, and finally a methanol bath [60]. Note that all the organic solvents were heated to 80°C before cleaning. It is generally believed that the GaAs surface is covered by a thin layer of native oxide. Therefore, following the organic solvent cleaning, the substrates were etched in dilute NH_4OH to remove the native oxide [61]. Just prior to the oxide deposition, the wafers were removed from the methanol bath and dried in a nitrogen jet. Care was taken to prevent the wafers from further contamination by dust or water.

ii) Deposition of TiO_2 thin films

The schematic representation of the CVD system is shown in Figure 3.1. The TPT source solvent was heated by a heating tape and controlled by a thermal controller. The temperature of the heating tape was kept at 100 ± 3°C for the purpose of attaining a desirable vapor pressure of the TPT source. The reaction chamber was heated by a R-F induction coil and the temperature was monitored by another thermal controller. The furnance temperature ranged from 200°C to 800°C, and this range was desired in studying the correlation between the film structure and the deposition temperature. The furnance was flushed with nitrogen and the

TPT was heated to 100°C before loading the samples. To prevent the possibility of explosion induced by the TPT vapor as heated, a two-way valve was used to direct the TPT vapor to the oil bath. After the samples were placed in the center zone of the reaction chamber, the two-way valve was switched on and the timer was set. It is usually observed that the deposition rate is dependent upon the substrate temperature and the bubbler flow rate. Considerable effort was made to achieve uniform deposition by adjusting main flow and bubbler flow rate. Special effort was also made to study the effect of oxygen deficiency by intentionally depositing the TiO_2 in an oxygen ambient [62].

iii) Annealing of the films

A variety of heat treatments were carried out on the films to study the effects of annealing on the properties of the films and those of the TiO_2-GaAs interface. Annealing at 400°C, 500°C, and 600°C with different periods of time was studied. In the light of the understanding of the effects of annealing ambient on the silicon-silicon dioxide ($Si-SiO_2$) interface properties, both oxygen and nitrogen ambients were considered. The results will be discussed in the fourth chapter.

iv) Metallization

An NRC Model 3116 vacuum coater system was used to perform the vacuum deposition. Indium or a gold-germanium allow was selected to form the back ohmic contact to n-type GaAs. A detailed review of ohmic contacts to III-V compound semiconductors has been given by Ridout [63]. A metal mask of 0.8cm x 0.8cm area was used for ohmic contacts. The evaporation was performed at a vacuum of approximately 4×10^{-6} Torr. The

field plate (or gate electrode) evaporation is similar to the ohmic contact evaporation, except that aluminum was generally used and the metal mask was an array of circular dots 10 mils in diameter. The thickness of the metal films is not critical, but a thickness of 0.5 - 1.0 microns for the back contact and at least 0.3 microns for the field plate were generally used. The MIS device fabricated by following the steps described above is schematically shown in Figure 3.2

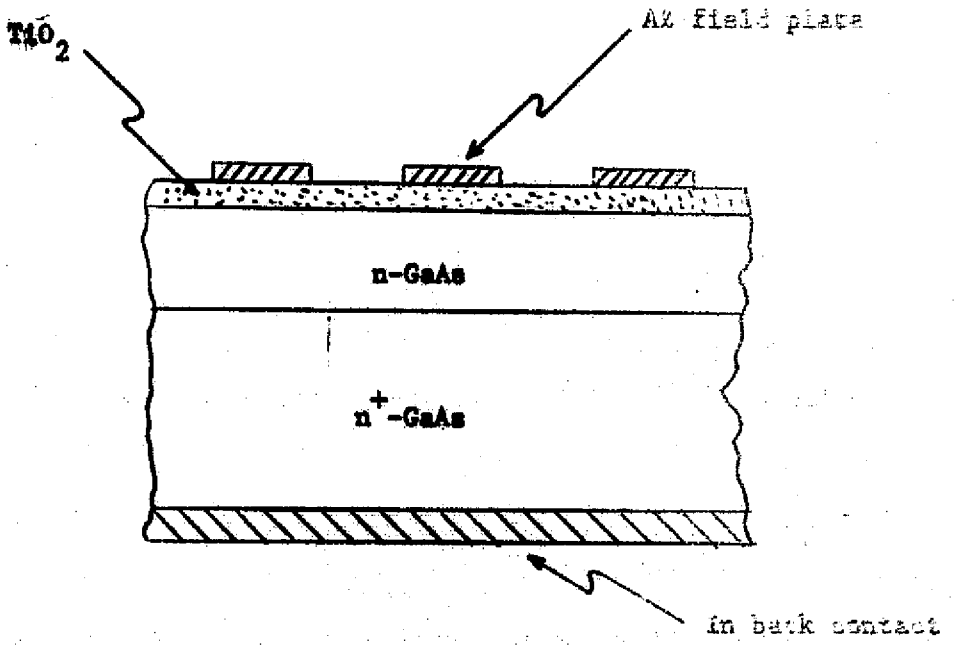

Figure 3.2. Schematic illustration of the Al-TiO_2-GaAs structure

3.3 X-ray Diffraction

It is widely accepted that the structure of the thin films will affect their electrical properties. Tremendous differences in the conduction process and the band structure between crystalline and amorphous materials have been observed [13,64]. Therefore, the structure of the as-grown TiO_2 films is of fundamental importance in this work. The X-ray diffraction instrument used for this structural study is composed of a Philips high angle spectrometer goniometer with type 42202, Philips water cooled diffraction unit, and a Philips electronic circuit panel as shown in Figure 3.3 The spectrometer goniometer is a device to measure the angle 2θ as required by the Bragg formula. The usable range of the goniometer is from -38° to 160° (2θ), which is large enough for the purpose of this study. The X-ray is generated by using Cu-Kα as the target and Ni as the filter. In order to prevent any peaks generated by the substrate, the TiO_2 films were deposited on amorphous fused quartz. Films deposited at different temperatures were investigated. The results of the X-ray diffraction will be given in Chapter 4.

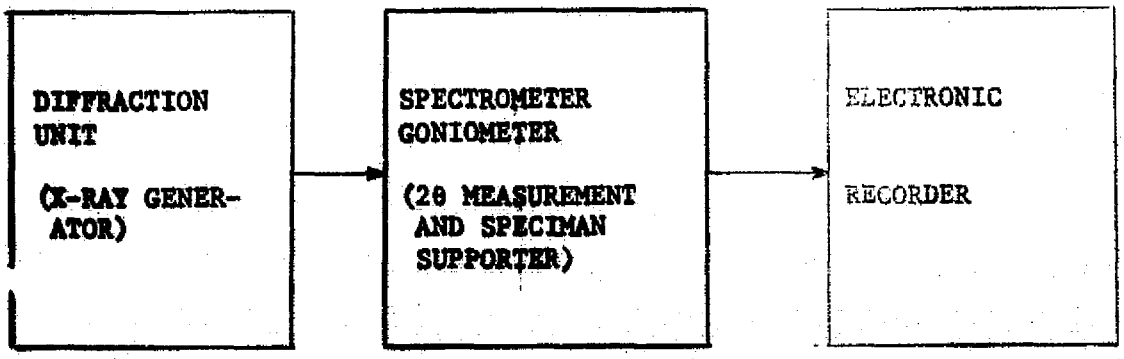

Figure 3.3. Block diagram of the X-ray diffractometer

3.4 Optical Measurements

In the study of thin films on substrates, three different optical methods of investigation are available [65]. These are: (1) photometric measurement of incident and reflected or transmitted rays to determine the optical constants and absorption peaks to obtain information concerning composition and structure of the materials, (2) polarization measurement of the reflected light to determine the optical constants of the reflecting surfaces and to measure the thickness of the films on substrates, (3) interference measurement to determine the film thickness and/or surface structure. The first will be covered in Section 3.4.2, and the second in Section 3.4.1.

3.4.1 Ellipsometry

Ellipsometry, which may be characterized as reflection polarimetry or polarimetric spectroscopy, is the measurement of the effect of reflection on the state of polarization of light [66]. Such measurement is interpreted to yield the optical constants of the reflecting material or, when the reflecting material is a film-covered substrate, the thickness and optical constants of the films. Detailed discussions of the theories involved are available elsewhere [65-67]. The fundamental principles which facilitate an understanding of the measurement will be discussed here.

It is well known that a wave of elliptical polarization can be decomposed as the sum of a p wave, which is in the plane of incidence, and a s wave, which is normal to the plane of incidence. In general, reflection causes a change in the relative phases of the p and s waves and a change in the ratio of their amplitude. More specifically, the state of polarization of the wave will change under reflection. The effect of reflection is characterized by the angle Δ, which is associated

with the change in phase, and the angle Ψ, the arctangent of the factor by which the amplitude ratio changes. Ellipsometry is the measurement of Δ and Ψ, which contain the characteristics of the reflecting surface. Once Δ and Ψ are determined, the optical constants and the thickness of the films can be subsequently determined.

The ellipsometer used in this study is the Gaertner Ellipsometer Model L119. A schematic representation of the ellipsometer is shown in Figure 3.4. The light source used in this study is a He-Ne laser with a wave length of 6328 Å. The incident beam is transmitted in sequence by the polarizer (either a Nicol or a Glan-Thompson prism) and the compensator (a mica quarter wave plate). The azimuthal orientations of these devices determine the relative amplitudes and phase difference between the p and s components of the incident beam. The orientations are adjusted so that the difference in phase just compensates that which results from reflection; thus Δ is measured. The plane-polarized reflected beam is then transmitted by the analyzer to a telescope and detector. The analyzer is then oriented to extinguish the reflected beam. This extinction setting measures Ψ.

A Fortran IV program adpated from McCrackin's work [68] is used in this study to perform the complicated calculations required to analyze the measurement. The results of this measurement technique will be given in Chapter 4.

3.4.2 Optical Absorption Measurements

Optical absorption is considered to be a versatile technique in solid state materials research. Not only the optical constants, such as

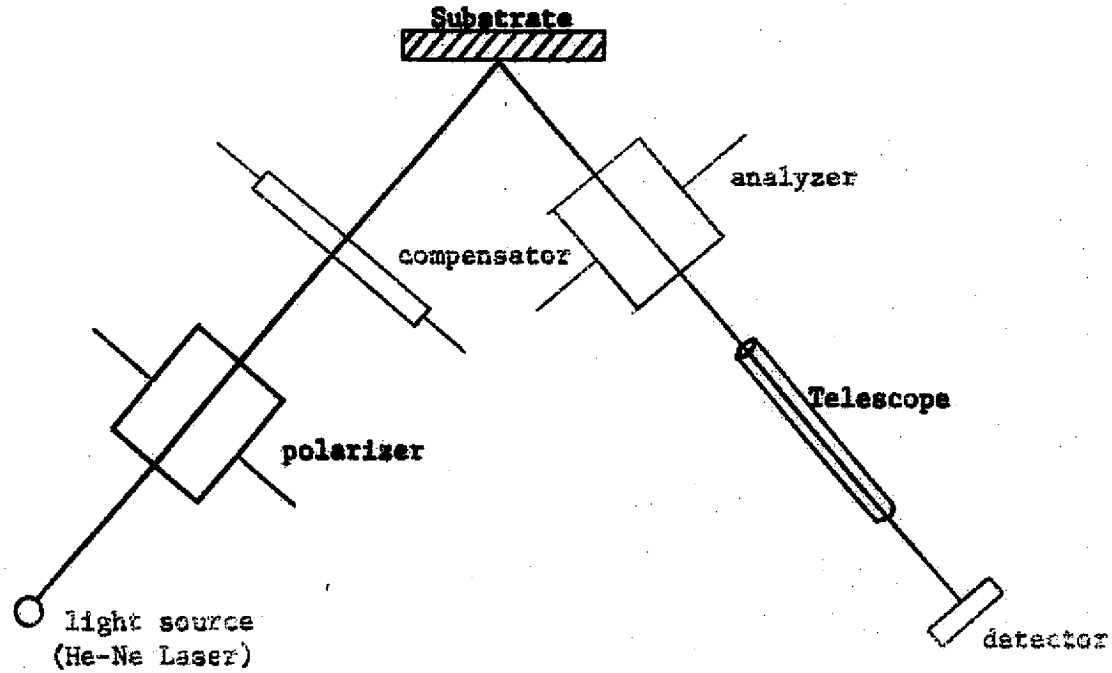

Figure 3.4. Schematic representation of the Gaertner Ellipsometer Model L119

the dielectric constant, refractive index, and absorption coefficient, but also the band structure of the materials can be studied. By appropriately plotting absorption coefficient (α) versus photon energy ($\hbar\omega$), one can determine whether the material has a direct-band gap or an indirect-band gap [1]. Moreover, optical absorption is applied to study the localized states in the gap of amorphous solids [55,58,64,69]. Figure 3.5 shows the optical region of the electromagnetic spectrum and the corresponding transitions [70]. It is apparent that the electronic transitions of interest cover the range of the visible and near ultraviolet (UV) regions. The instrument used in this study is the Cary 14 spectrophotometer. The spectrum is plotted on the recording charts supplied by Graphic Controls Corporation. The recording charts have absorbence as the ordinate and the wavelength as the abscissa. The absorbence (A) is defined as $\log(I_o/I)$, where I_o and I are the intensity of the incident and transmitted waves, respectively.

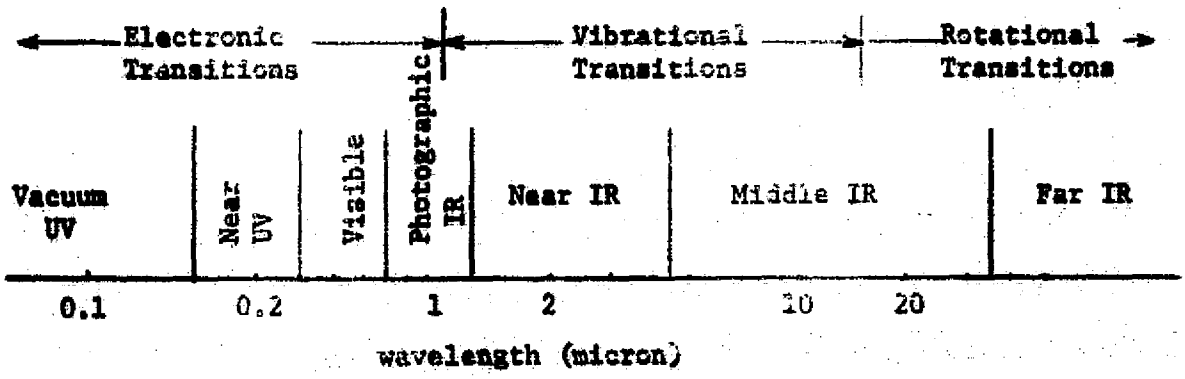

Figure 3.5. The optical region of the electromagnetic spectrum and corresponding transitions

The TiO_2 films to be studied are deposited on SI-UV fused quartz, purchased from ESCO Optics Products. The SI-UV fused quartz shows excellent transmission in the visible and UV region. In order to get an absorption spectrum for the TiO_2, three runs are required for each sample. The first run gives the air versus air spectrum, i.e., the base line. Secondly, the spectrum associated with the fused quartz substrate versus air is obtained. The last run supplies the TiO_2 coated fused quartz versus air data. The absorption spectrum of TiO_2 itself is then obtained after some manipulations.

3.5 Device Tests

Following metallization, the MIS (or MIM) devices are subjected to various tests for the purpose of investigating the properties of the insulator and of the semiconductor-insulator interface. Current-voltage (I-V) measurements are utilized to meet the first purpose. The capacitance-voltage (C-V) measurement is by far the most frequently employed technique in determining the interface properties due to the simplicity of fabricating test devices, the ease of making (automatic) measurements, and the large amount of information that can be obtained as described in Chapter 2. The determinations of the conductivity type, impurity concentration, minority carrier lifetime, interface state density, and the properties of the insulator itself are among its most general applications. The experimental procedures and set-up to do these studies will be discussed in this section.

3.5.1 C-V Measurements

Figure 3.6 shows the block diagram of the C-V system used in this study. The system basically consists of a HP7035B X-Y Recorder and a

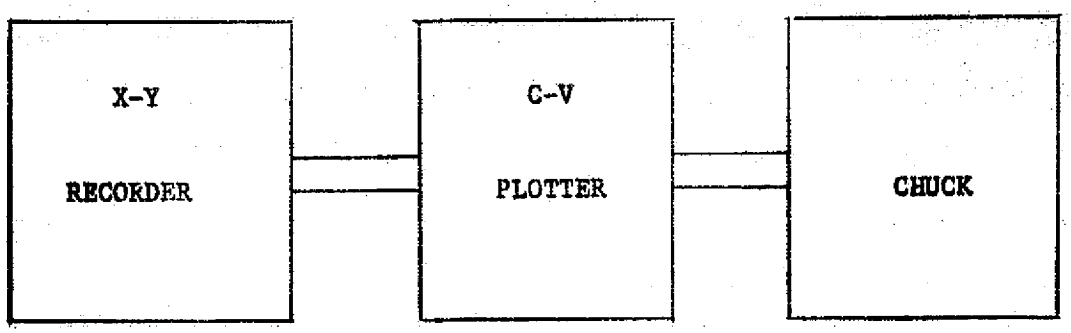

Figure 3.6. Block diagram of the C-V system

Model 410 C-V Plotter purchased from Princeton Applied Research Corporation. The C-V plotter primarily includes a variable d-c voltage for bias stressing, a 1 MHz capacitance meter, and a ramp generator. By operating the Model 410 in conjunction with the X-Y recorder, a real time C-V plot is readily obtained. The C-V plotter has other capabilities as well, including that of direct a-c parallel conductance measurements and transient (lifetime) measurements. Figure 3.7 is a simplified block diagram of the Model 410 C-V Plotter. The 1 MHz oscillator provides a 15 mV rms modulation drive to the device under test. It also provides a reference signal to the phase sensitive detector (PSD). The mode switch can control the phase of the drive so that the demodulation is with respect to either the capacitive current component or the conductance current component, whichever mode is selected. The modulation drive is applied to the substrate of the MIS wafer. The resultant current signal at the gate is applied to the probe and connected to the Model 410 input. Following several stages of amplification, the signal is applied to the PSD where it is demodulated, producing a d-c level proportional to the level of the signal of interest. After certain stages of d-c amplification, the signal is

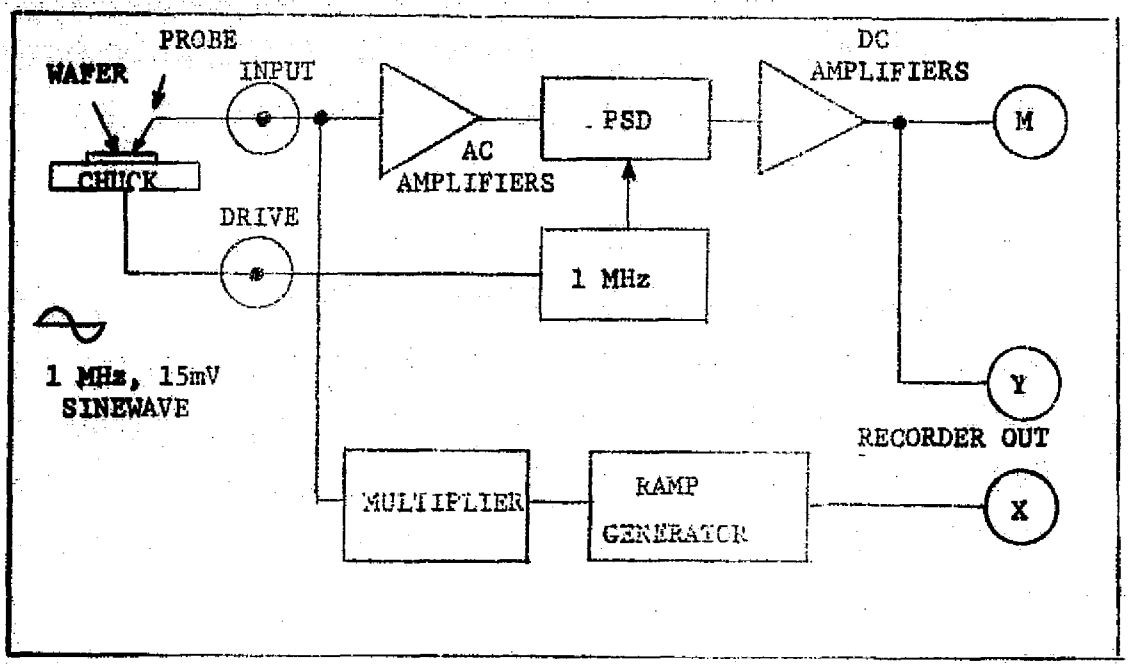

Figure 3.7. Block diagram of Model 410 C-V plotter

used to drive the capacitance meter and the Y axis output. The ramp is developed by a ramp generator circuit controlled by the Ramp Generator Controls. This provides the X-axis drive to the X-Y recorder and also the ramp that is applied to the device under test.

The capacitance value at a specific d-c bias can be read either from the panel meter or from a digital voltage meter (DVM) which is connected to the Y axis of the recorder. The C-V plotter can be either in a single trace mode or in a retrace mode. Of course, the instrument is operated in the retrace mode to facilitate the hysteresis effect studies.

3.5.2 I-V Measurements

The purpose of the d-c conduction study is (1) to understand the conduction level and therefore the dielectric properties of TiO_2 films,

(2) to calculate the resistivity of the TiO_2 films, and (3) to investigate whether the conduction mechanism is bulk-limited or electrode-limited. Figure 3.8 shows the block diagram of the experimental set-up. The Keithley Model 602 Electrometer is a solid state battery operated instrument which measures a wide range of d-c voltage, current, resistance, and charge. The electrometer has twenty-eight current ranges from 10^{-14} ampere to 0.3 ampere full scale. Current conduction through the MIM (or MIS) structures was measured by applying a voltage between the back contact and the field plate and observing the total current flow through the Keithley 602 Electrometer. The applied voltage is increased with an increment of 0.01V at low voltages and with an increment of 0.1V at higher voltages so that ohmic conduction in the lower voltage region can be detected. The experimental results will be shown in Chapter 4.

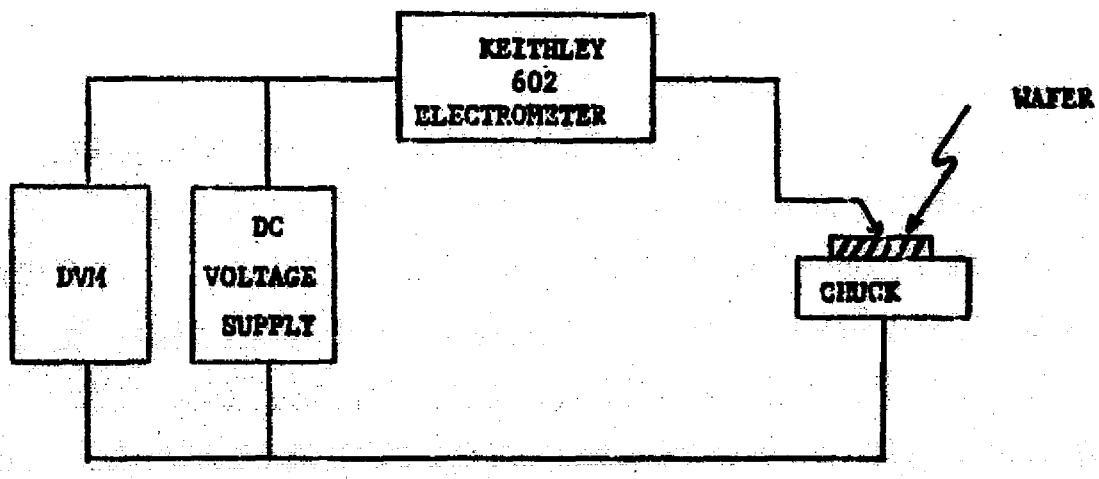

Figure 3.8. Block diagram of the set-up for I-V measurements

4. EXPERIMENTAL RESULTS AND DISCUSSION

The material developed in this chapter will first present the results of various studies, followed by an analysis of the experimental data based on the theories developed in Chapter 2.

The physical and optical properties of TiO_2 films are presented first. Then comes the core of this thesis which is the electrical properties of the MIS (or MIM) structure. Special emphasis is placed on the semiconductor-insulator interface properties, which are monitored by capacitance-voltage measurements.

4.1 Physical Properties of TiO_2 Thin Films

The titanium dioxide thin films prepared in this study exhibit brilliant color hue because of the high refractive index. It is known that much of the early effort to characterize TiO_2 was due to its attractiveness for optical coatings. Presently, these properties are being exploited in the fabrication of solar cells [71]. The "as deposited" films show either deep blue or golden yellow, depending on the depositing temperature and period of depositing time. The films show good uniformity which can be easily controlled by adjusting the flow rate of TPT source. However, it is generally observed that controllability covers a wider range for lower substrate temperatures than for higher ones. Excellent uniformity extending over the whole area of a 1" diameter silicon wafer has been achieved for the film deposited at 200°C.

As described in Chapter 3, an ellipsometer using a helium-neon laser with wavelength 6328 Å as the light source is employed to determine the refractive index and film thickness. The refractive index so determined

ranges from 1.84 to 1.9 for films deposited at 200°C and from 1.9 to 2.1 at 400°C. The increase of the refractive index with respect to the increase of deposition temperature is reasonable since the films become denser at higher temperature, as will be corroborated later. These values are lower than the value of 2.6 reported for single-crystal rutile [10, 72]. However, values from 1.96 to 2.6 have been reported [13,22,73] for the index of refraction of thin film TiO_2. Also, the index of refraction for other oxides in thin film form are reported to be lower than for bulk oxides [74]. The TiO_2 films adhere to silicon, gallium arsenide and fused quartz substrates very satisfactorily. No peeling or cracking has ever been observed.

X-ray diffraction analysis was employed to analyze the structure of the TiO_2 films using copper K^{α} radiation. Much of the early effort was made in studies of films deposited on gallium arsenide substrates. Unfortunately, the appearance of the characteristic peaks associated with the GaAs substrate and sometimes those of the spurious peaks due to the Cu K^{β} or Fe K^{α} radiations make the interpretation of the data difficult. This difficulty was later overcome by depositing TiO_2 on fused quartz, which is known to be amorphous. The useful information shown below was extracted from this kind of study. Figure 4.1 shows the diffraction pattern of the TiO_2 deposited at 400°C. The small peak occurring at $2\theta=25.4°$ was identified to be associated with a d-spacing of 3.51 Å after adjusting the scale factor as shown in Figure 4.2. This line was then characterized to be due to the titanium dioxide anatase phase. A similar peak was observed for a film deposited at 300°C, as shown in Figure 4.3. The diffraction pattern of a 275°C film, as shown in Figure 4.4, is interesting since no peak was observed at first glance. However,

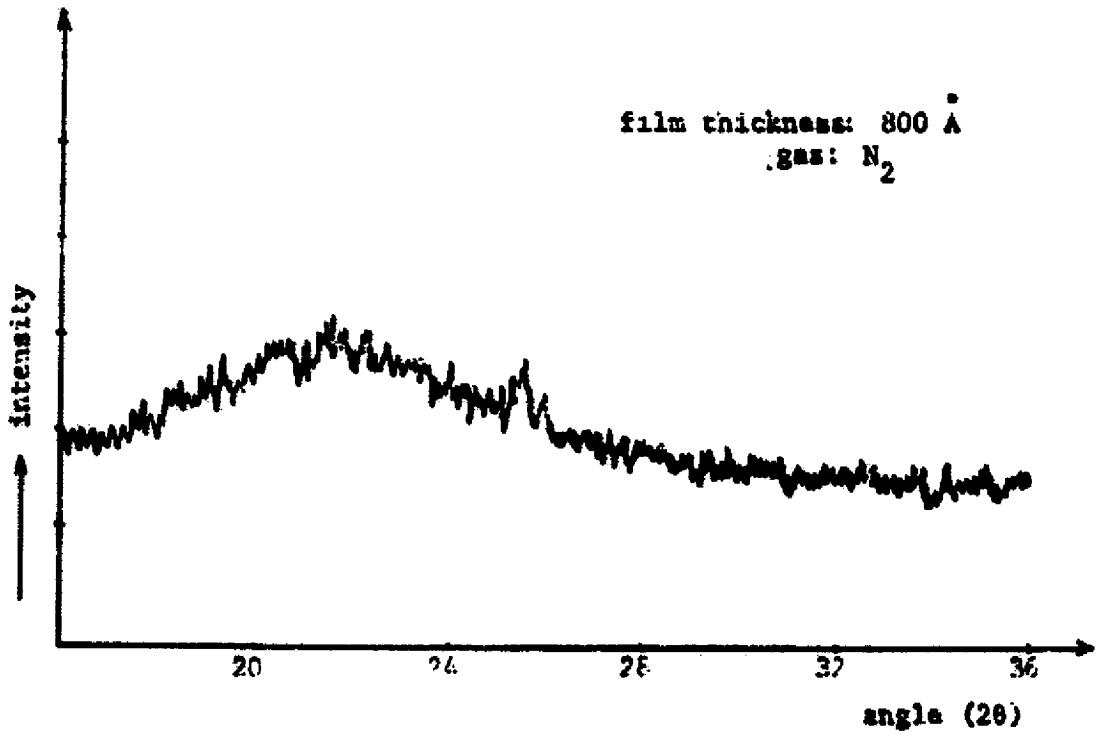

Figure 4.1. Diffraction pattern of the TiO_2 thin film deposited at 400°C

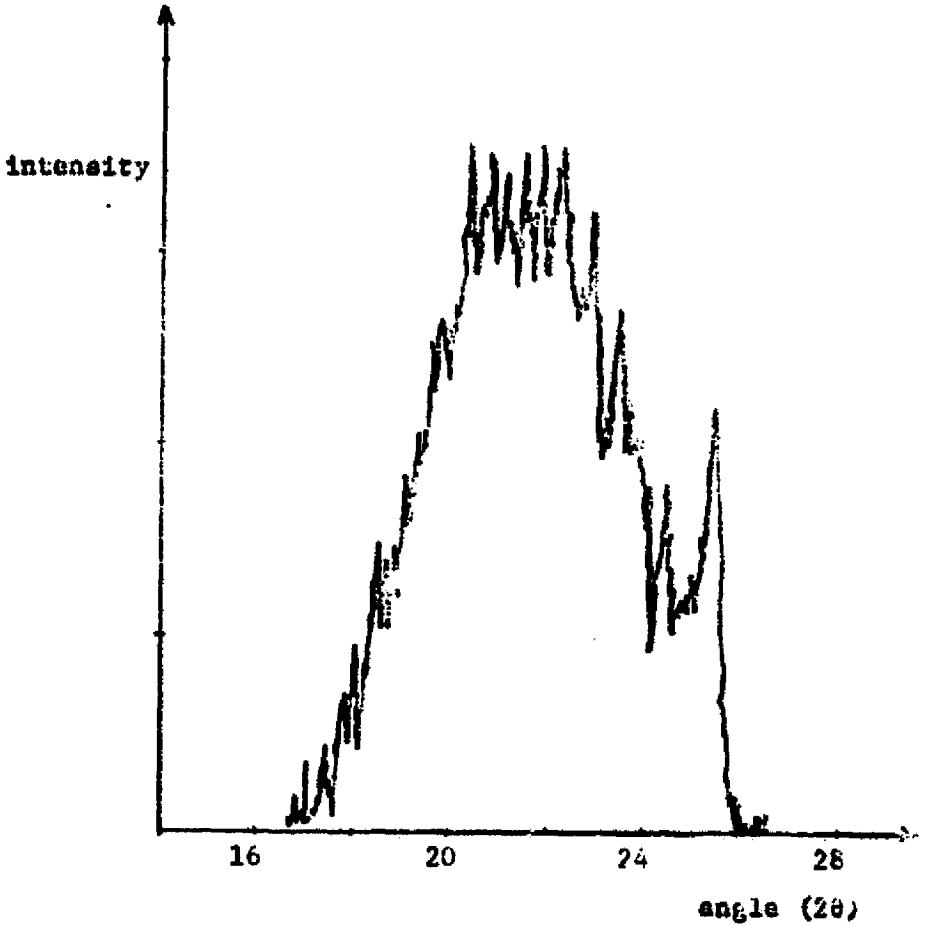

Figure 4.2. Illustration of the peak at 2θ=25.4°

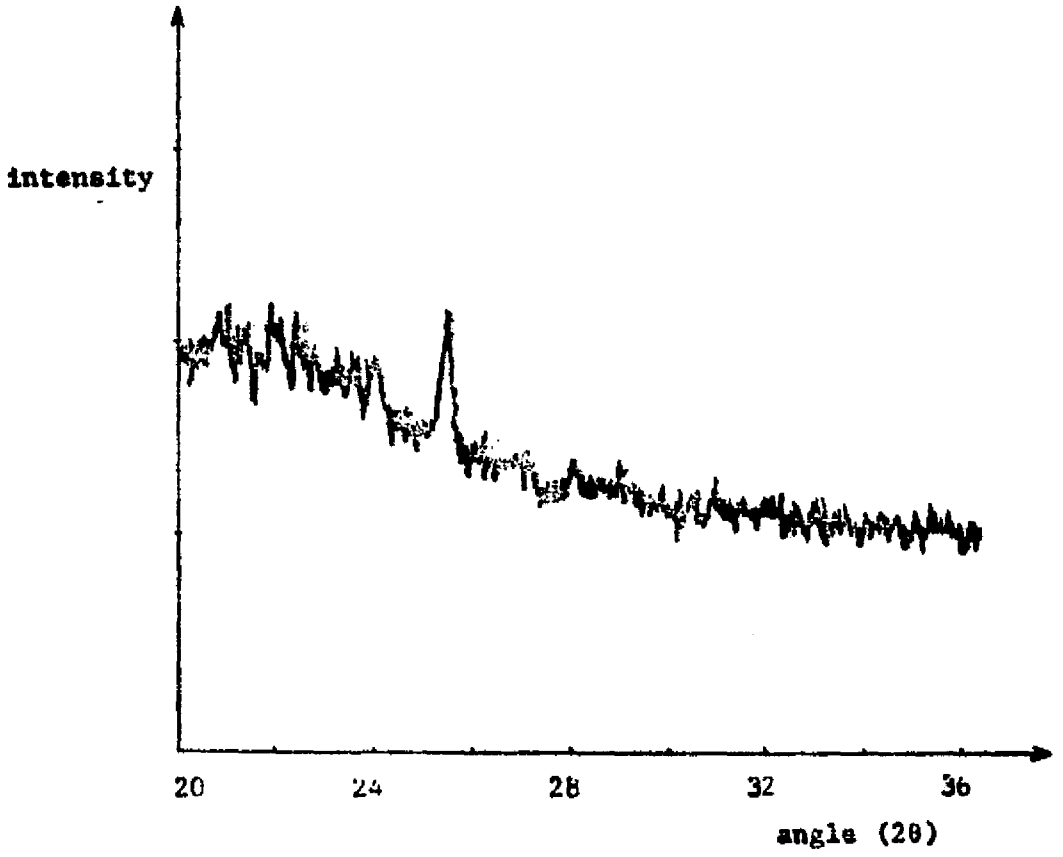

Figure 4.3. X-ray diffraction pattern of the TiO_2 film deposited at 300°C

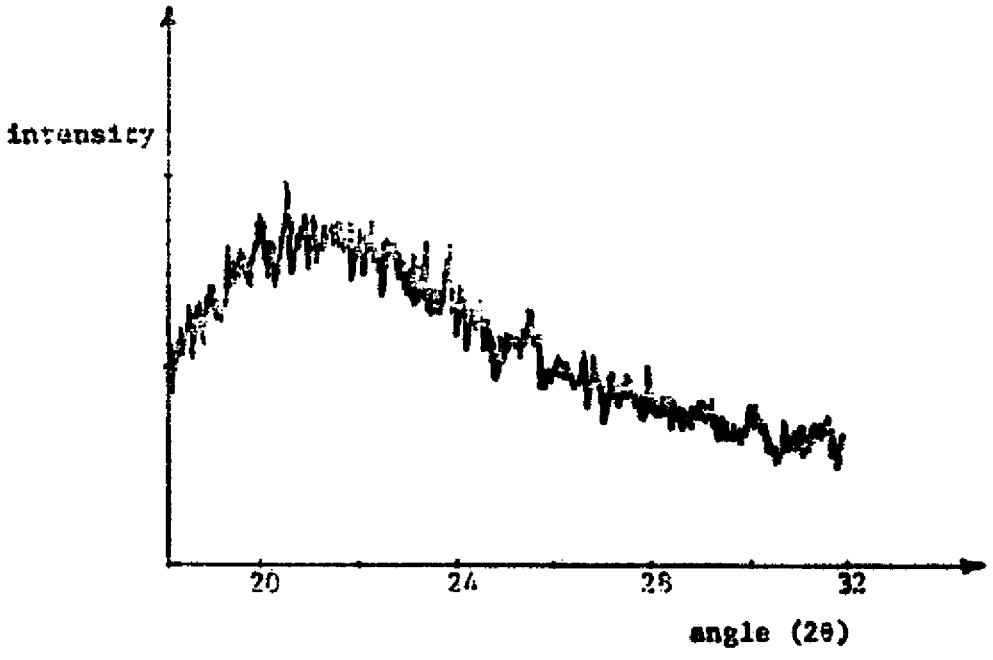

Figure 4.4. Diffraction pattern of the TiO_2 film deposited at 275°C

an extremely weak peak corresponding to the anatase phase was finally characterized by means of the built-in counter on the diffractometer. Figure 4.5 reveals the amorphous characteristic of the film deposited at 200°C. The results are summarized in Table 4.1. It is seen that the

Table 4.1. Crystal structure of the films deposited at various temperatures

	Deposition temperature °C			
	200	275	300	400
Structure	Amorphous	Amorphous + anatase	Anatase + amorphous	Anatase

transition from anatase to the amorphous phase occurs at 275-300°C. This kind of phase transition has been found by other workers. Fitzgibbons, et al. [22] gave a somewhat higher transition temperature for their chemical-vapor-deposited TiO_2 films. The result shown here agrees satisfactorily with those reported elsewhere.

A dielectric film is required to be etchable in liquid etchants at room temperature for electronic applications. Crystalline titanium dioxide is known to be considerably impervious to chemical attack [22]. The etchability of TiO_2 was determined for films deposited on GaAs at various temperatures. As a matter of fact, nearly half of the effort of the X-ray diffraction study was exploited to help solve the etching problem. Titanium dioxide films as deposited at 400°C were found to be impervious to any kind of acids except HF. However, the etching rate in 49 percent HF was too low to be practically acceptable. More unfortunately, the results indicate that most of the films etched in 49 percent HF leave a residue. These facts have seriously imperiled the

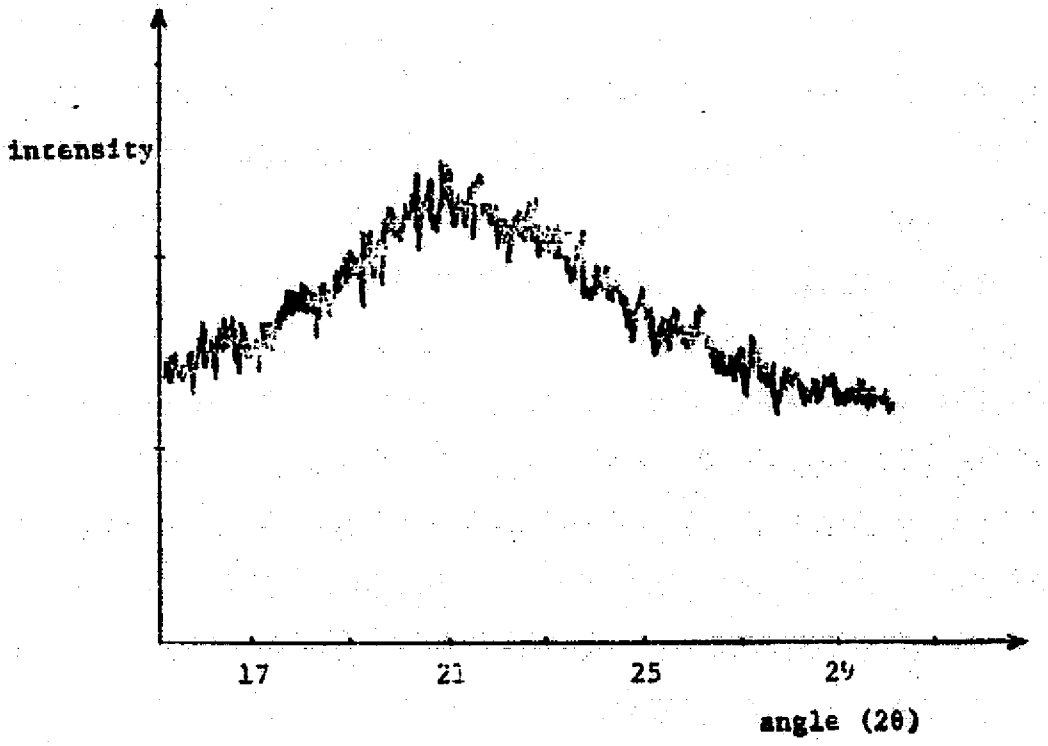

Figure 4.5. X-ray diffraction pattern of the TiO_2 film deposited at 200°C

possibility of electronic applications of TiO_2 films. In an effort to solve these problems, studies were begun at lower deposition temperatures. Following a series of experiments, satisfactory results were achieved. Titanium dioxide films deposited at 200°C can be easily etched in 49 percent HF. These results are in accord with the X-ray diffraction study, if one notices that amorphous material is always easier to etch than crystalline material. The results are also consistent with those of Fitzbiggons [22] and Yokozawa [75]. The results of etch susceptibility are summarized in Table 4.2.

Table 4.2. Etch susceptibility of TiO_2 films

Deposition temperature	Etchant and etch rate			
	49% HF	100% Hcl	100% H_2SO_4	85% H_3PO_4
200°C	very rapid	slow with residue	very slow	very slow
300°C	slow, residue	No	slow residue	slow, residue
400°C	slow residue	No	No	very slow residue

Finally, the effect of annealing on the physical properties of the TiO_2 films is presented. Most of the films deposited in this study were annealed at either 400°C or 500°C in nitrogen or in nitrogen/oxygen mixtures. More than a 12 percent decrease in thickness for the 200°C films was observed after 60 minutes of annealing. The thickness decrease for 400°C films was not detectable within the accuracy of the ellipsometer measurement. A slight increase in refractive index was also noticed for films deposited at 200°C and 400°C. Differences between annealing in nitrogen and annealing in various percentages of oxygen were undetectable as far as the physical properties were concerned.

4.2 Optical Absorptions

The primary purpose of optical absorption is to calculate the optical band gap of the TiO_2 films as well as to investigate whether the crystalline or polycrystalline TiO_2 is a direct-band gap or indirect-band gap material, as these factors are of the utmost importance to the carrier transport in the material. The basic functional dependences of the absorption coefficient on the photon energy have been discussed in Chapter 2. Based on the functional dependences, one can determine whether or not a crystalline (or polycrystalline) solid is a direct-band gap material by plotting α^2 (or $\alpha^{1/2}$) versus $\hbar\omega$. A typical result of this study for the films deposited at 400°C is shown in Figure 4.6. Notice that the absorption increases rapidly as the wavelength of radiation is smaller than 0.38 μm. An optical band gap of 3.7 eV, based on Figure 4.7, is obtained. This band gap is considered to be associated with a direct band-to-band transition. Recently, the band structure of titanium dioxide by Daude, et al. [76] reveals that the lowest indirect transition (3.02 eV) is $X_1 \rightarrow X_1$. The present result of 3.7 eV is close to the first direct transition. Although a gap of 3.2 eV can be obtained by a direct extrapolation from Figure 4.6, it is not adopted due to the lack of theoretical justification.

The optical absorption spectra of the TiO_2 film deposited at 200°C is shown in Figure 4.8. This figure is then converted to Figure 4.9, on the basis of the theory derived in Chapter 2. A density-of-states energy gap of the order of 3.22 eV is obtained. The reported values of the optical gap of TiO_2 range from 3.65 eV to 3.96 eV [17,19]. Notice that these values are generally estimated from the absorption spectra. The degree of the accuracy of applying this estimation to an amorphous

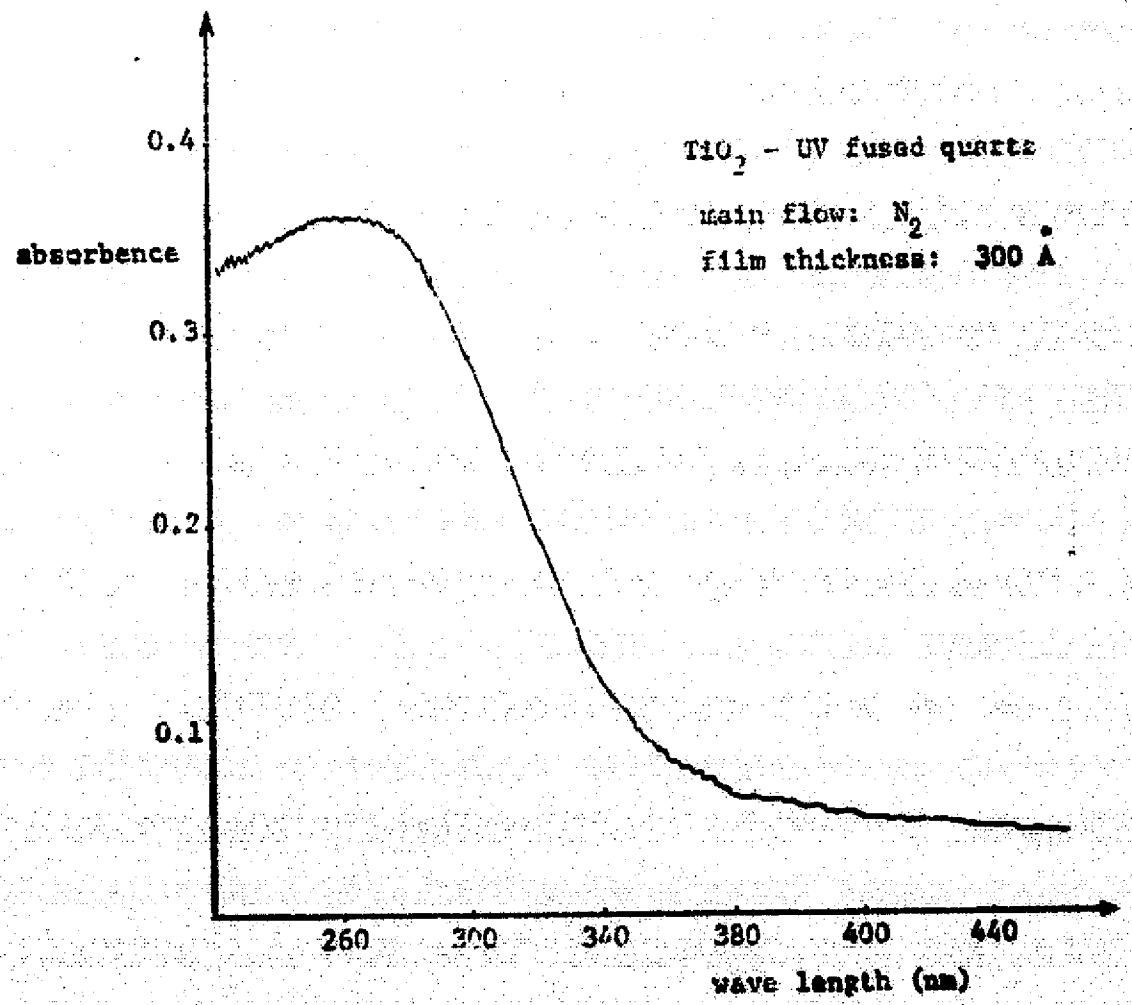

Figure 4.6. Absorption characteristic of the TiO_2 film deposited at 400°C

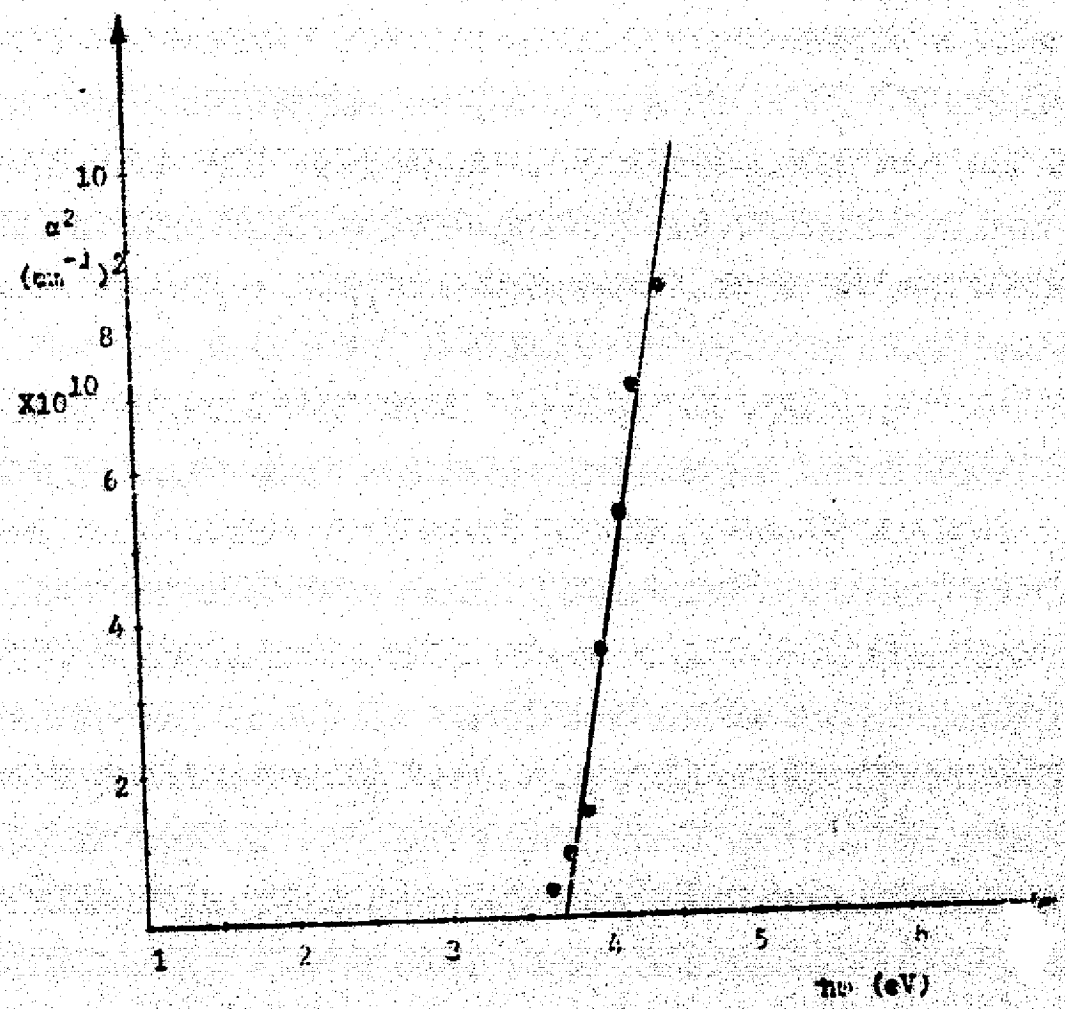

Figure 4.7. Dependence of α on $\hbar\omega$ of the TiO_2 film deposited at 400°C

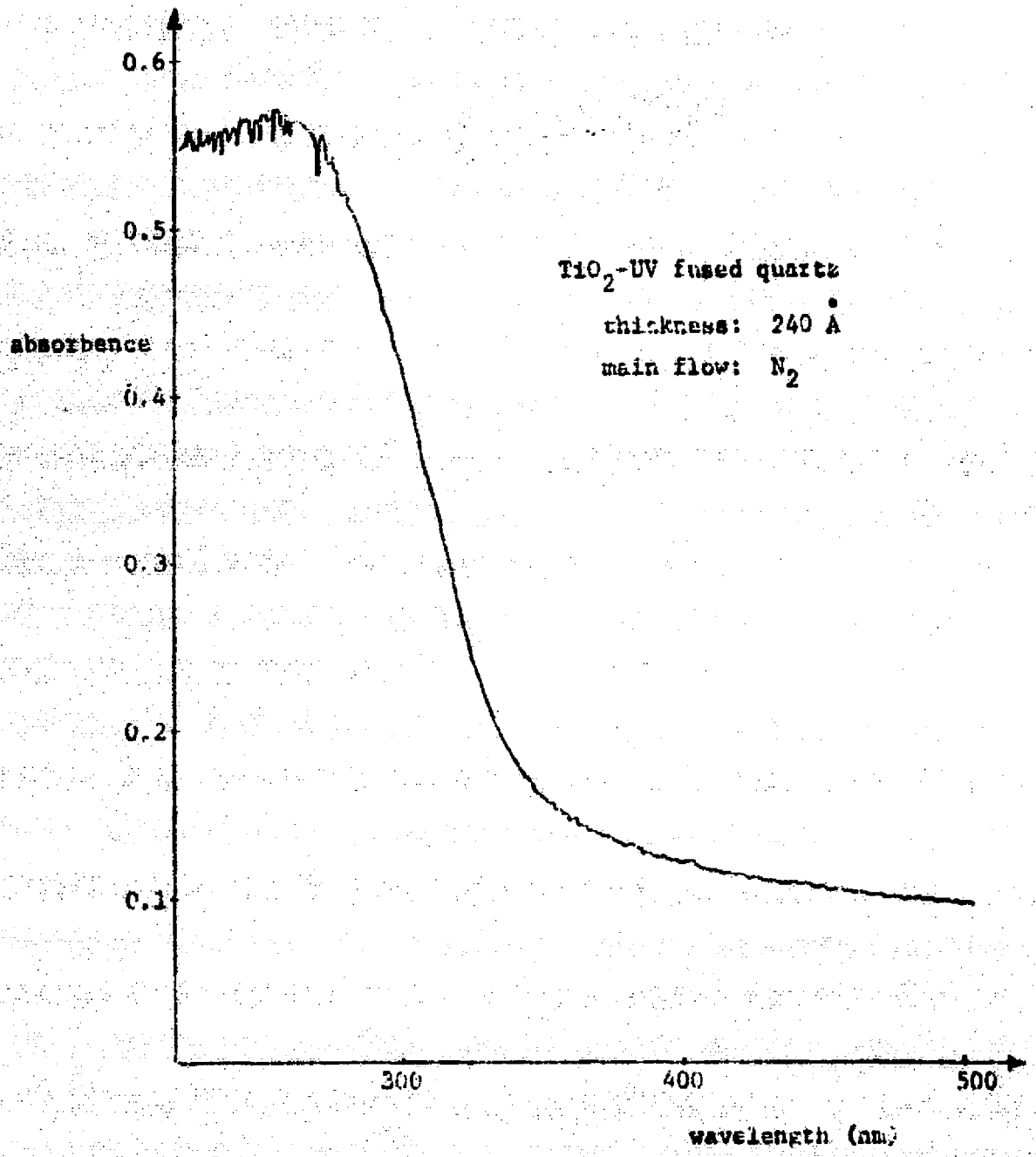

Figure 4.6. Absorption spectrum of the TiO_2 film deposited at 200°C

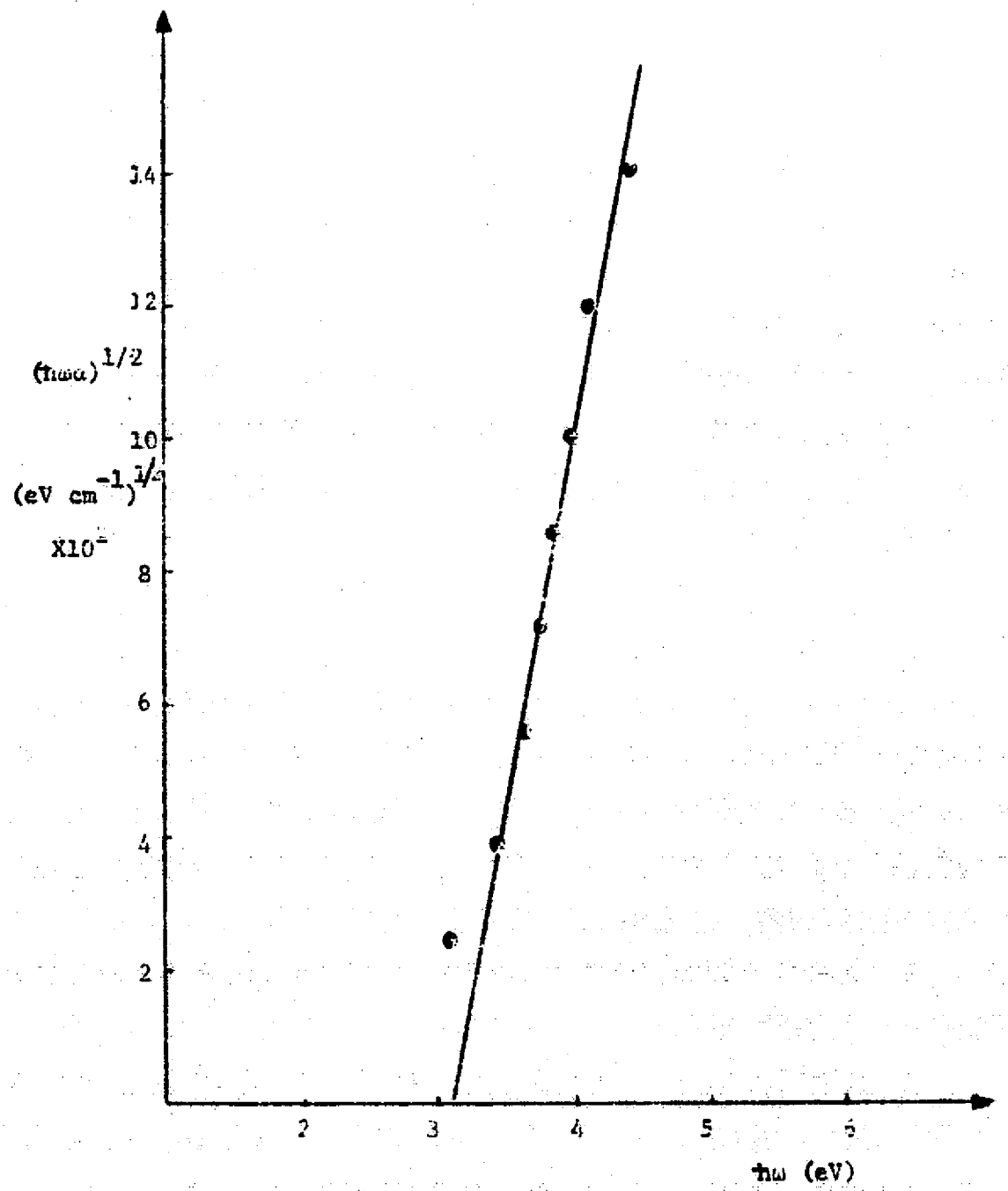

Figure 4.9. Dependence of $(\hbar\omega\alpha)^{1/2}$ versus $\hbar\omega$ of the amorphous TiO_2 thin film

solid is questionable. It is also interesting to note that a band gap of 3.75 eV is obtained if an α^2 versus $h\omega$ plot, as shown in Figure 4.10, is applied. Although the consistency with the literature is evident, the meaning of such a plot remains uncertain.

The absorption spectrum presented thus far are associated with the films, either polycrystalline or amorphous, of thickness smaller than 400 Å. The reason for utilizing such thin films is to prevent the spectrophotometer from operating under an overload condition. One of the spectra obtained from a thicker film (1000 Å) deposited at 500°C is shown in Figure 4.11. This diagram is especially plotted for both percent transmittance and absorbence. Certain absorption peaks which are not seen previously are present. The absorption peaks above 0.35 um are attributed to interference due to multiple internal reflection [22]. The absorption peak at the vicinity of 0.32 um is believed to be due to the band-to-band transition. Extrapolation beyond 0.32 um gives rise to a band gap of 3.90 eV. The optical gap estimated here is consistent with both that of Figure 4.7 and that of Fitzgibbons' [22]

4.3 Current-Voltage Characteristics

The d-c conduction level of the as-deposited TiO_2 films is generally high. In the study of conduction mechanisms, either a linear plot (I vs. V) or Schottky plot (log I vs. $\sqrt{V}$) is employed. A linear plot is used to detect the existence of ohmic conduction and also to calculate the resistivity, whereas the Schottky plot is employed to investigate whether a Schottky emission (electrode-limited) mechenism or a Poole-Frenkel (bulk-limited) mechanism is dominant. The linear plot of a titanium dioxide film deposited at 400°C in a nitrogen atmosphere is shown in

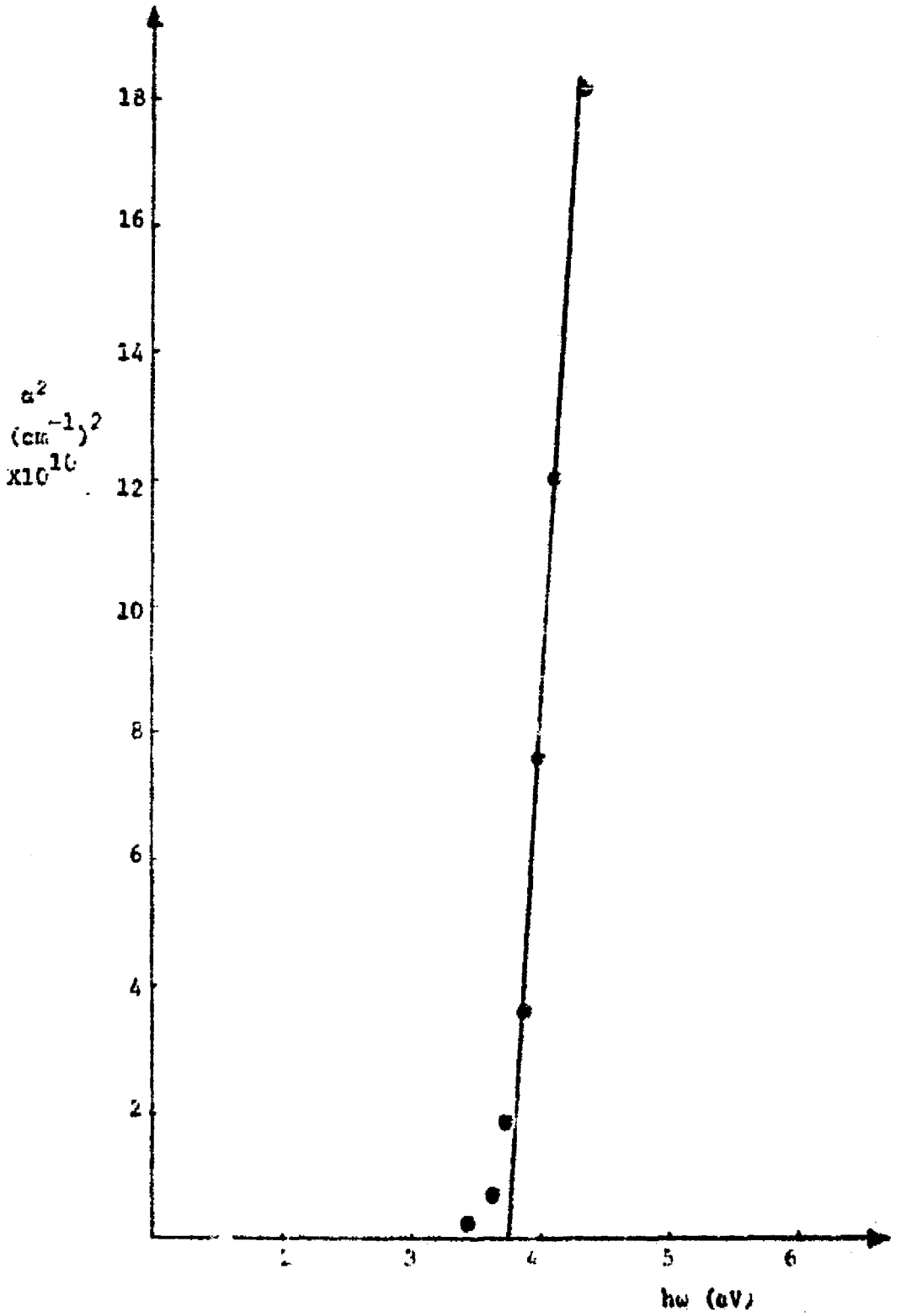

Figure 4.10. Dependence of α^2 versus hω of the amorphous TiO_2 film

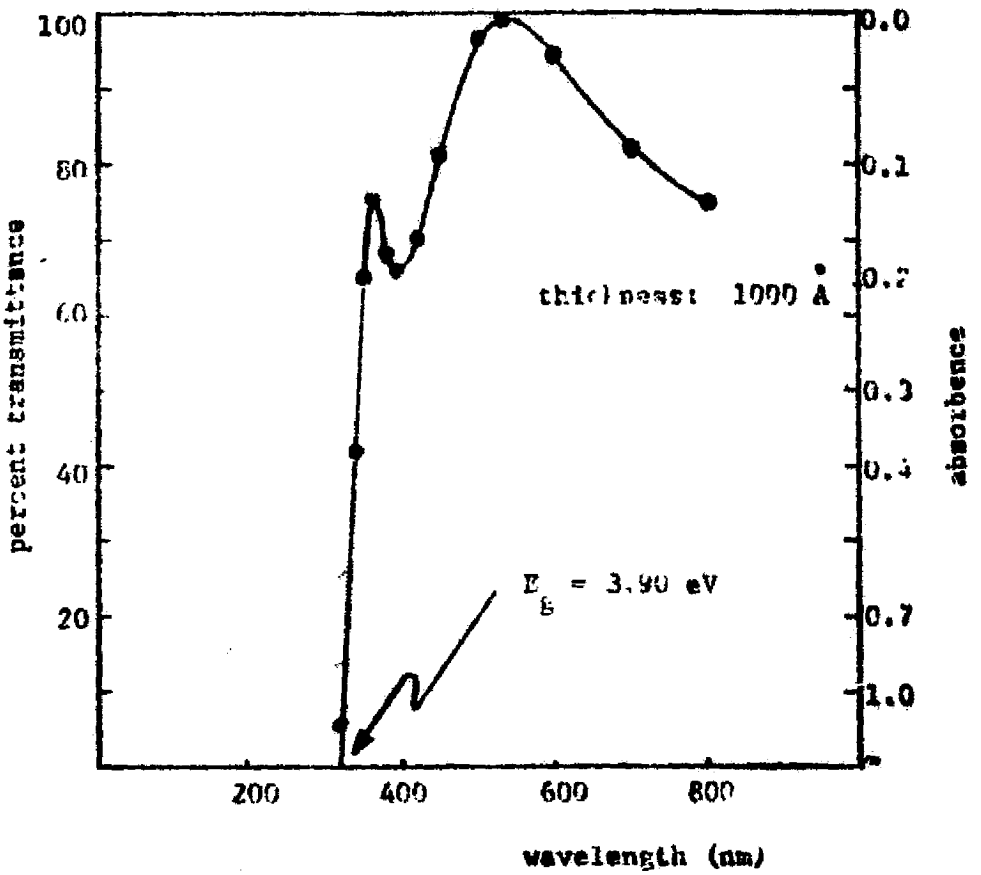

Figure 4.11. Transmittance characteristic of the TiO_2 thin film deposited at 500°C

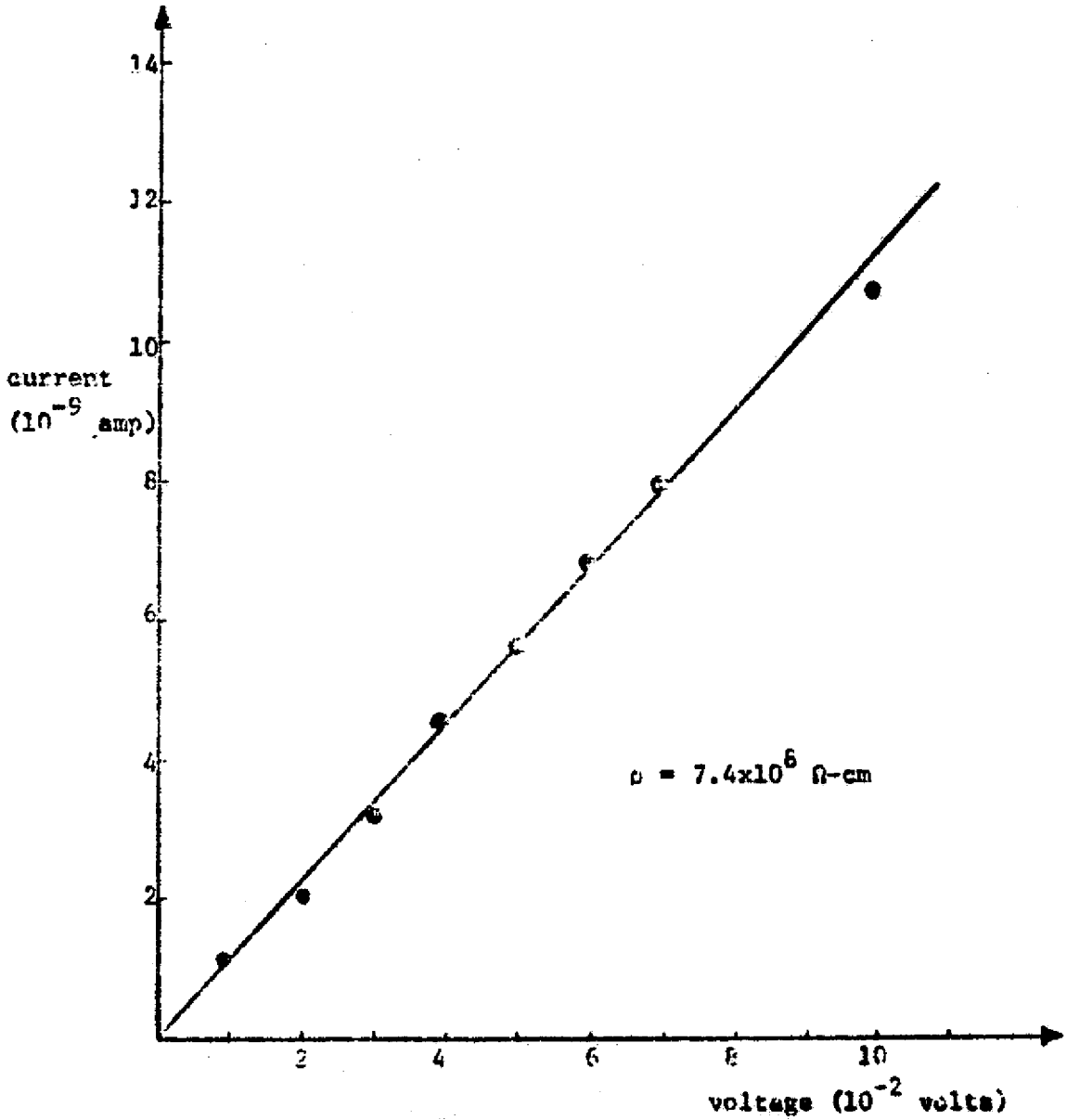

Figure 4.12. Ohmic conduction at low voltage of the 400°C TiO_2 thin film

Figure 4.12. The slope of the curve is calculated to correspond to a resistivity of 7.4×10^{6} Ω-cm. It is believed that the conduction mechanism in this ohmic region is attributed to the hopping conduction [77], which is a phonon assisted tunneling between neighboring sites, as illustrated in Figure 4.13. The Schottky plot fits the I-V characteristic quite well, as illustrated in Figure 4.14. The slope of this Schottky plot is 2.76, which is close to the theoretical value of 2.5, if the Poole-Frenkel mechanism is assumed dominant. This discrepancy is believed to be due to the inaccuracy in the measurement of the optical refractive index. Nevertheless, the conclusion that a bulk-limited Poole-Frenkel mechanism is responsible for the d-c conduction in this region is justified. If the applied voltage is further increased, a space-charge limited process finally becomes important.

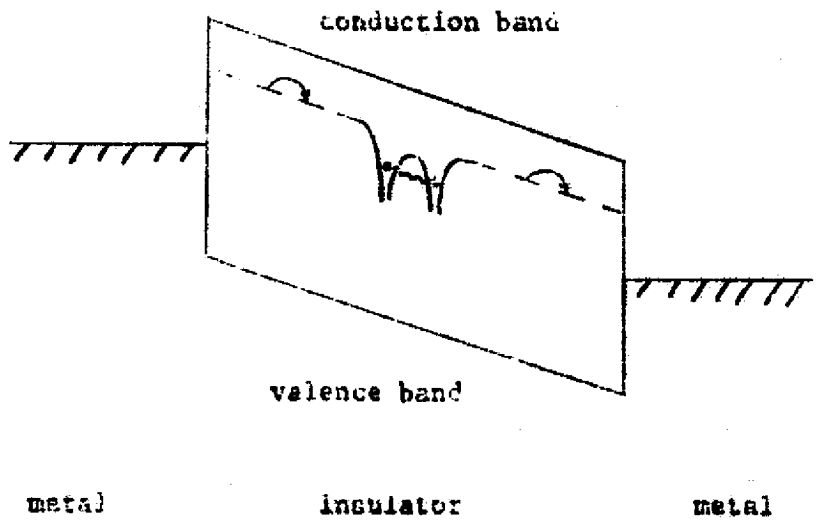

Figure 4.13. Illustration of the hopping conduction due to phonon assisted tunneling between neighboring impurity sites

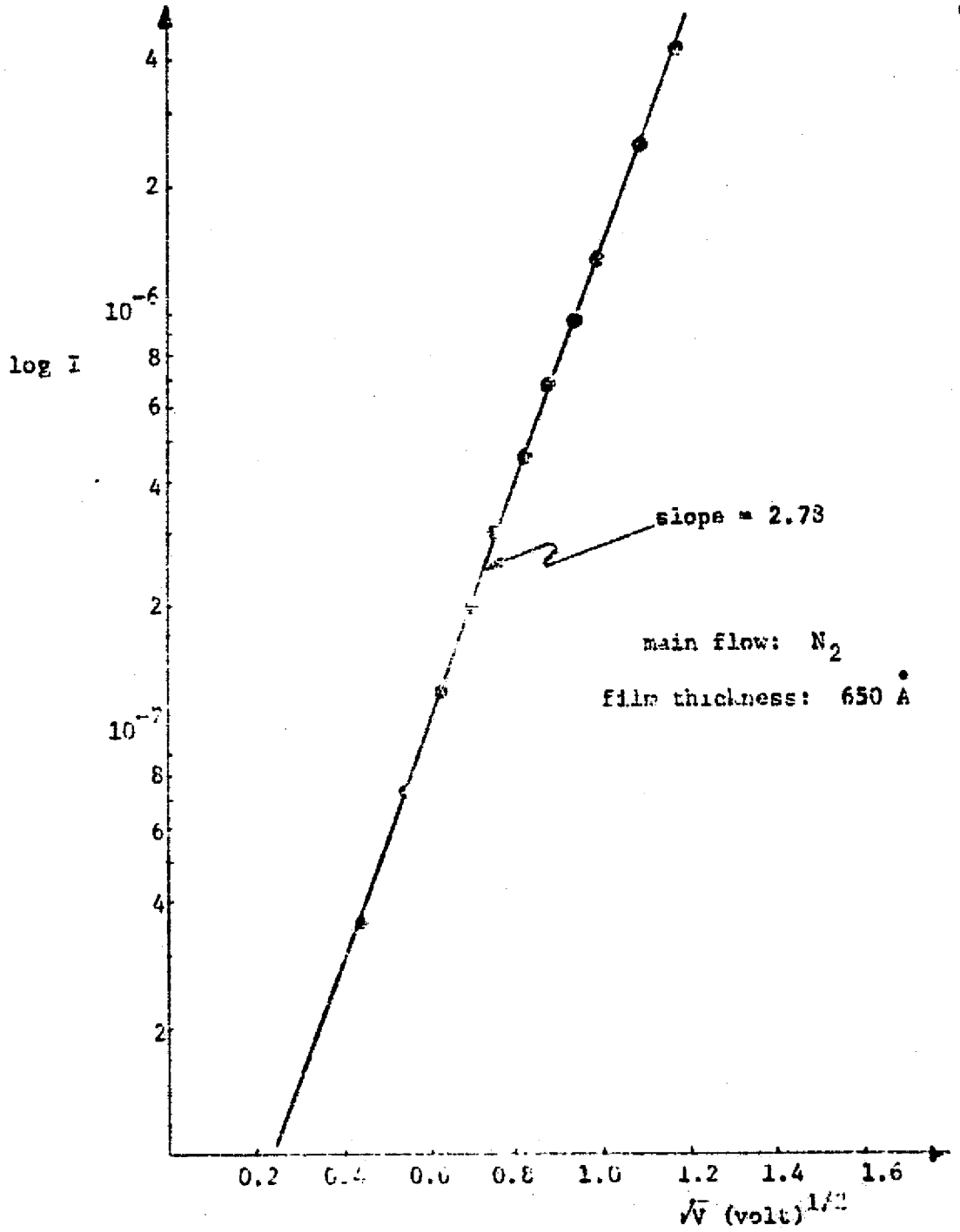

Figure 4.14. Schottky plot of the TiO_2 thin film deposited in N_2 at 400°C

Titanium dioxide films deposited in an oxygen atmosphere, which will undoubtedly increase the oxidation state, are also investigated. A Schottky plot of an as-deposited film is shown in Figure 4.15. It is interesting to notice that the conduction level of the film deposited in oxygen is decreased by two orders of magnitude as compared to that deposited in nitrogen. It has been proposed that the oxygen vacancy constitutes a donor state in titanium dioxide [78]. Consequently, the phenomenon observed here is plausible in that the oxidation effectively decreases the density of donor sites and subsequently decreases the density of free carriers arising from field-assisted ionization under bias. A resistivity as high as 5.7×10^{16} Ω-cm is calculated

The fact that Poole-Frenkel emission is the dominant mechanism in thin titanium dioxide film conduction has been identified by Harbison and Taylor [13]. The resistivity of single crystalline titanium dioxide (rutile phase) was reported to be 10^{15} Ω-cm [79]. Hada, et al. [80] reported the resistivity of thin film TiO_2, prepared by reactive sputtering, to range from 0.01 Ω-cm to 10^{11} Ω-cm depending on the oxygen partial pressure. Based on this review, the result of the present study is consistent with those reported elsewhere. Further increase in the resistivity is of course possible if annealing in an oxygen atmosphere is performed.

4.4 Capacitance-Voltage Characteristics

The capacitance-voltage measurement is made to investigate the existence of an inversion channel and to calculate the surface state density. A systematic C-V study is actually based on the following considerations.

(1) Does the crystalline structure of the film affect the TiO_2-GaAs interface properties.

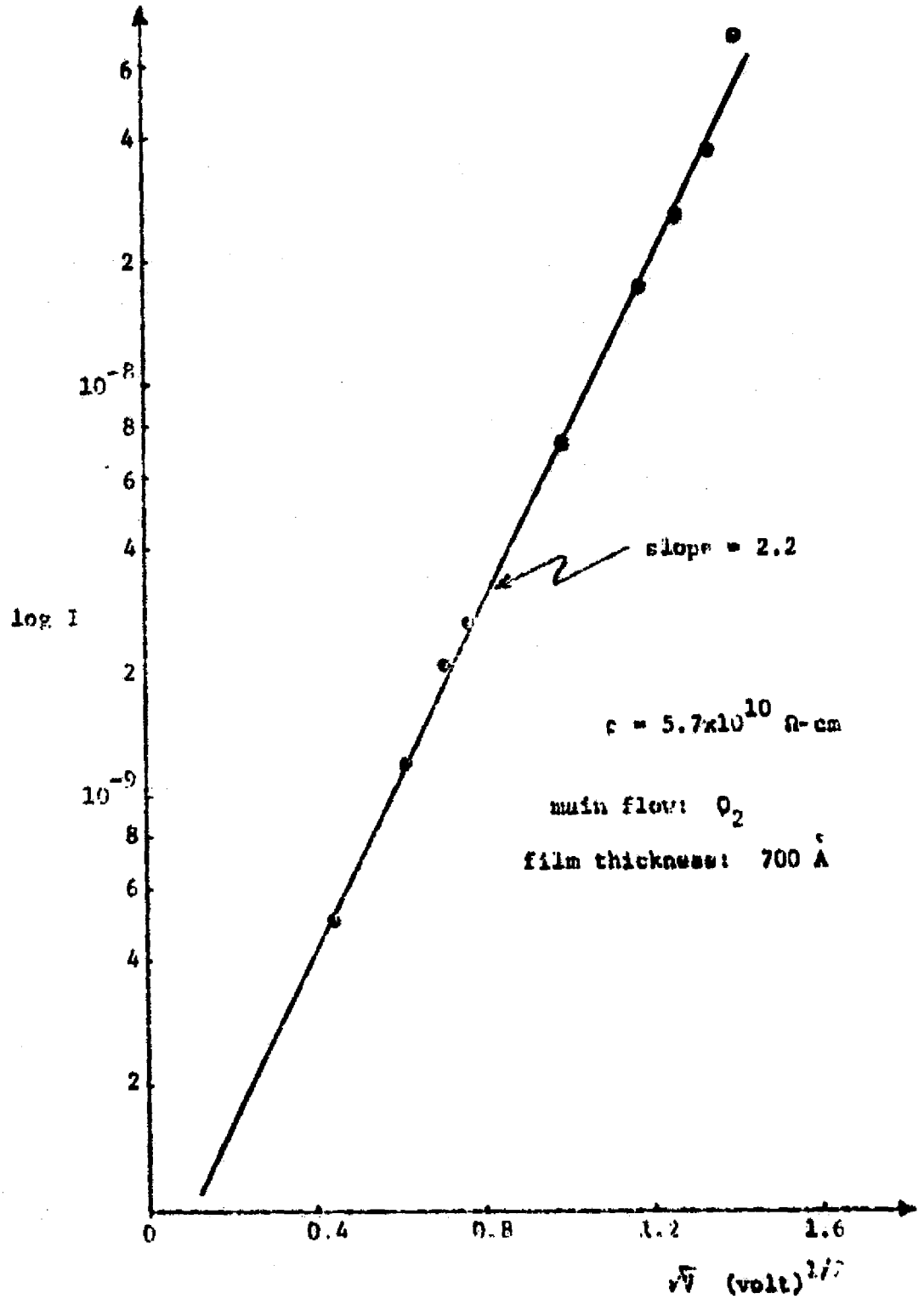

Figure 4.15. Schottky plot of the TiO_2 thin film deposited in O_2 at 400°C

(2) It has been observed, as presented in Section 4.3, that titanium dioxide deposited in an oxygen atmosphere shows higher oxidation state than that deposited in nitrogen. It is intuitive to ask whether or not the oxidation state will play any important role in surface state density reduction or inversion channel formation.

(3) Based on our experiences in silicon technology, it is well understood that annealing generally lowers the interface state density. Is this effect also true in the case of TiO_2-GaAs interface? Also, does it make any difference in the interface properties between annealing in O_2 and in N_2?

A variety of investigations have been performed to answer the questions described above. To avoid the coupling of several variables, e.g., temperature, annealing atmosphere, etc., all samples in the same set are deposited allowing only one variable at a time to be changed. Under such a complete and systematic study, very good results have been achieved. Those of great importance for the present interest will be qualitatively described as follows:

(1) The films deposited in the oxygen atmosphere are better than those deposited in the nitrogen as far as the interface property is concerned. This result arises from comparing Figure 4.16 with Figure 4.17. It has been pointed out that titanium dioxide deposited in the oxygen atmosphere shows a higher degree of oxidation, as described in Section 4.3. Consequently, it is reasonable to draw the conclusion that films with a higher oxidation state show better interface

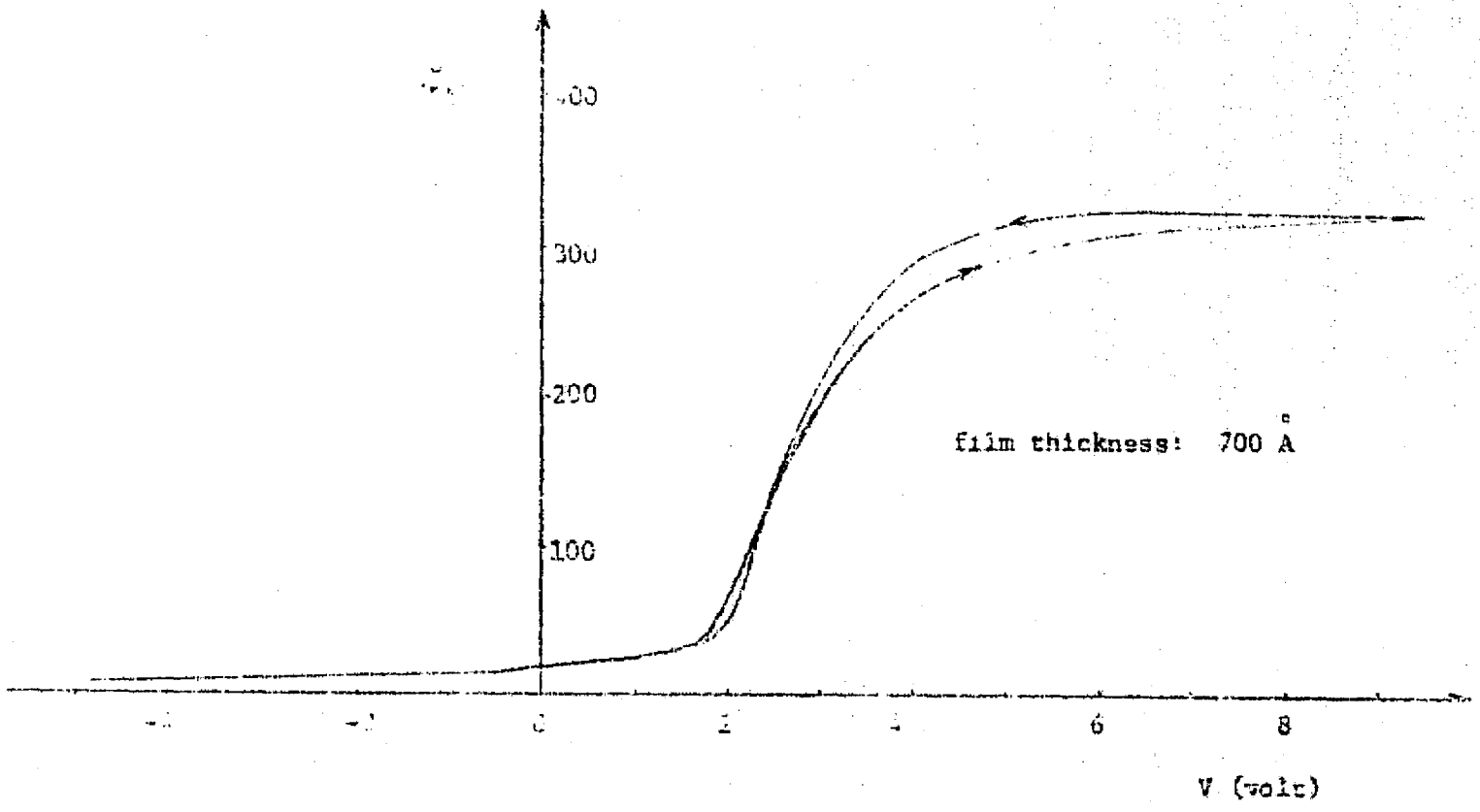

Figure 4.16. The C-V characteristic of an Al-TiO_2-GaAs capacitor with TiO_2 deposited at 400°C in O_2 atmosphere

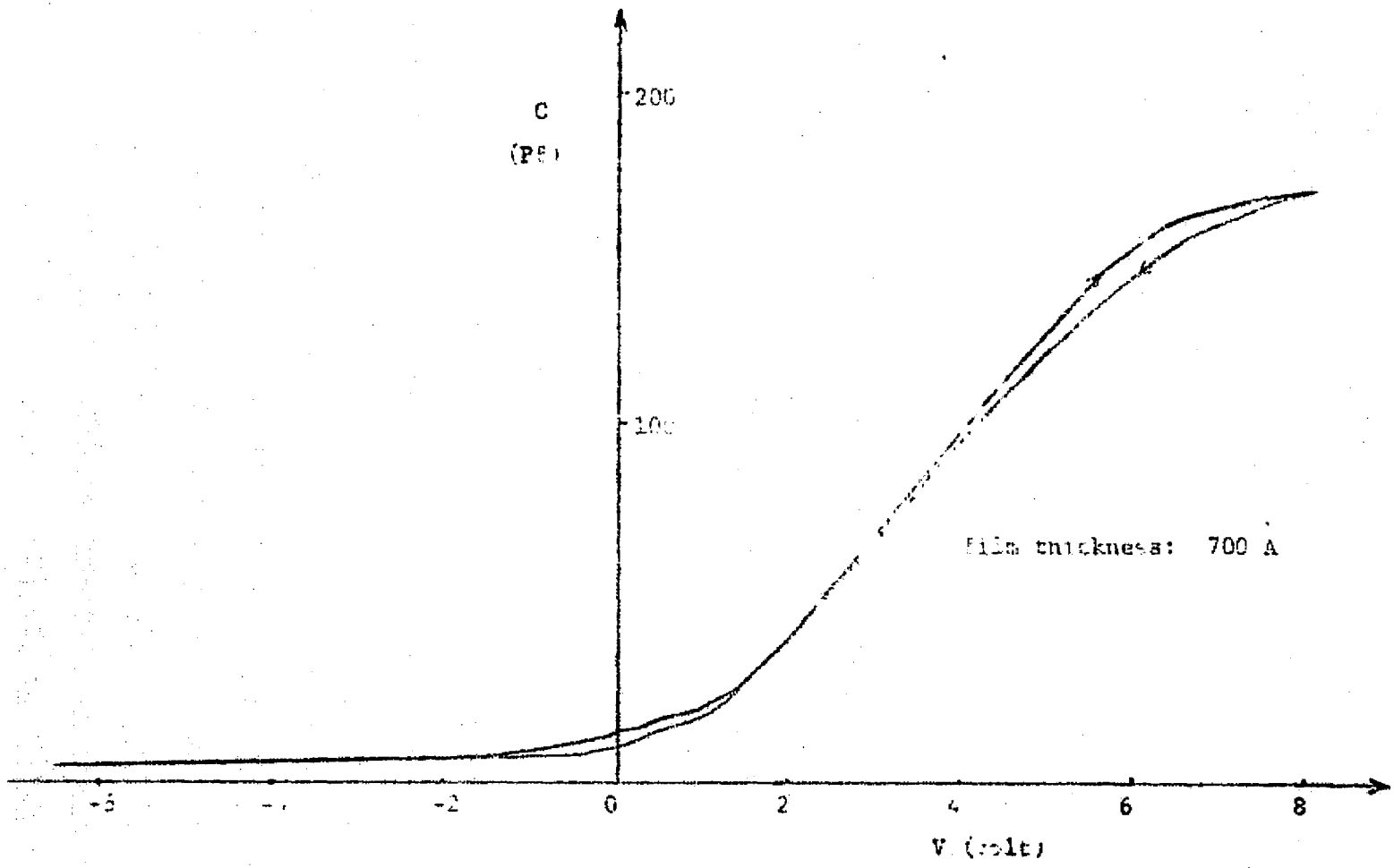

Figure 4.11 The C-V curve of an Al-TiO_2-GaAs MIS capacitor with the TiO_2 films deposited at 400°C in the N_2 atmosphere[2]

properties. If this conclusion is true, it is also plausible to infer that the films annealed in oxygen would have higher quality. In effect, this phenomenan has been observed as illustrated in Figure 4.18.

(ii) If the films are not deposited in an oxygen atmosphere, annealing is generally required in order to achieve an inversion layer.

(iii) It is also observed that the longer the period of annealing time, the better the quality of the films. Annealing for at least 40 minutes is generally required to have any detectable effect on the interface property. It is generally believed, however, that As will evaporate from the GaAs surface at temperatures higher than 500°C, and subsequently accumulate at the insulator-semiconductor interface if titanium dioxide is a diffusion mask for As atoms. Such an arsenic layer will undoubtedly induce trapping centers at the interface, although the detail of the trapping mechanism is unknown. Based on this, the constructive and destructive effects are assumed to reach a compromise. The period of annealing time ranging from 40 to 120 minutes is recommended.

(iv) Titanium dioxide films deposited at 400°C offer good resistance to ion migration at room temperature based on the negligible hysteresis (at room temperature) associated with the C-V curve, as demonstrated in Figure 4.16-4.18. A rudimentary bias-temperature stress (B-T) study also supports this conclusion. It is well understood, based on the knowledge of silicon technology, that silicon nitride offers better ion-migration

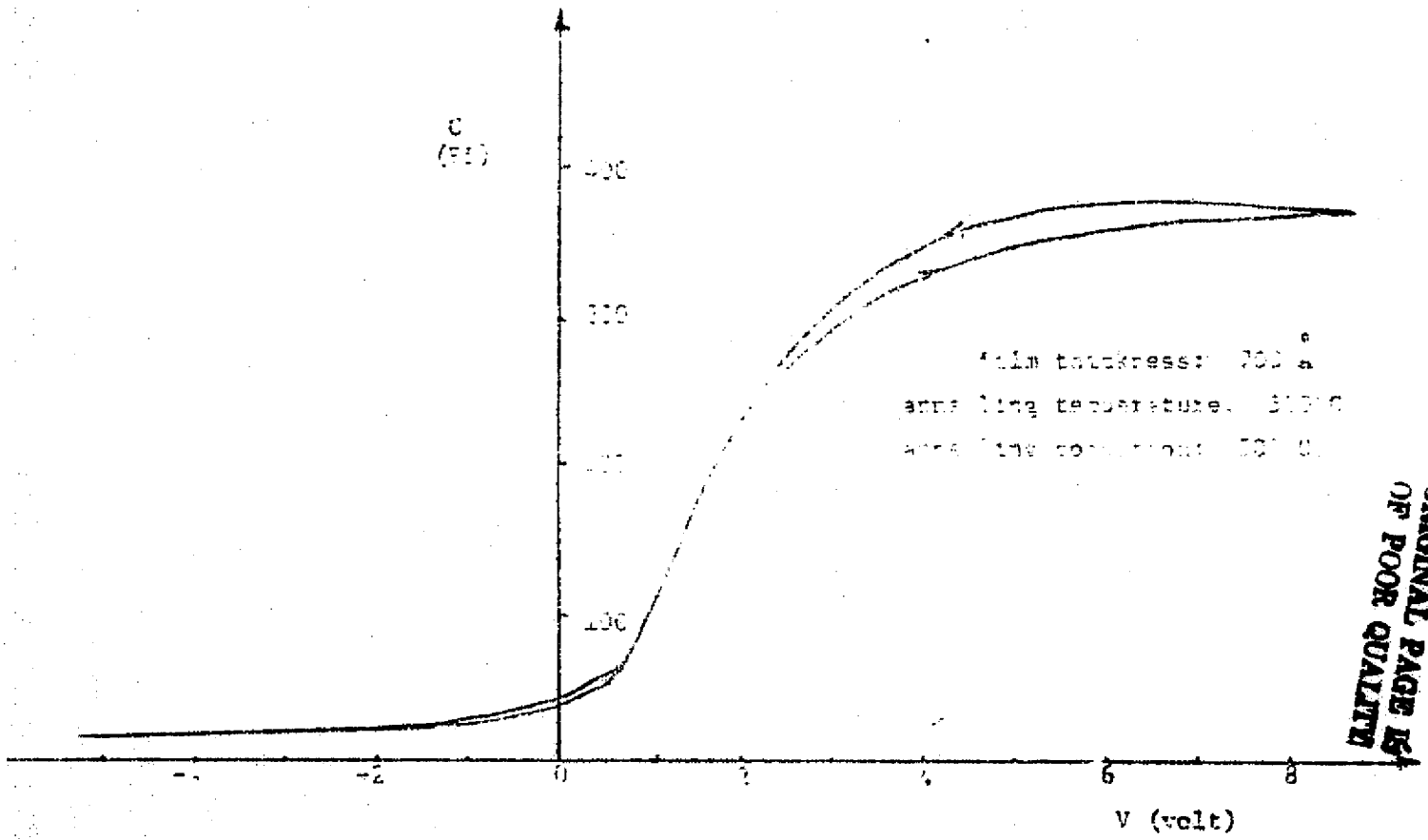

Figure 4.13 The C-V characteristic of an Al-TiO_2-GaAs MIS capacitor with the TiO_2 films deposited at 400°C and the device annealed at 500°C, 50 percent O_2

protection, and of course, a better diffusion or ion-implantation mask than silicon dioxide. The result of the present study makes titanium dioxide substantially comparable to silicon nitride in this respect.

(v) Hysteresis is usually observed in the accumulation region. Such a hysteresis is either due to fast surface states [18] or due to the high conduction level of the oxide. This is because most of the applied bias drops across the oxide as the semiconductor is in the accumulation region.

(vi) The properties of the TiO_2-GaAs interface are believed to be determined partly by the material characteristic and partly by surface preparation conditions. Figure 4.19 shows a C-V characteristic of an Al-TiO_2-S_i MIS capacitor. It is apparent that a well-defined inversion and accumulation region are shown. However, in Figure 4.20, the inversion region is not achievable. If the conduction levels of the TiO_2 films on Si and on GaAs are assumed to be the same, one can conclude that the surface state plays an important role in the formation of an inversion layer. More discussions on this will be presented later.

The insulator-gallium arsenide interfaces investigated by other workers were mostly reported to exhibit difficulty in achieving an inversion layer [33]. However, an acceptable inversion layer can be easily obtained in the present study if the films are deposited at about 400°C. Of technological importance in device application is that the inversion channel can also be achieved for the films deposited

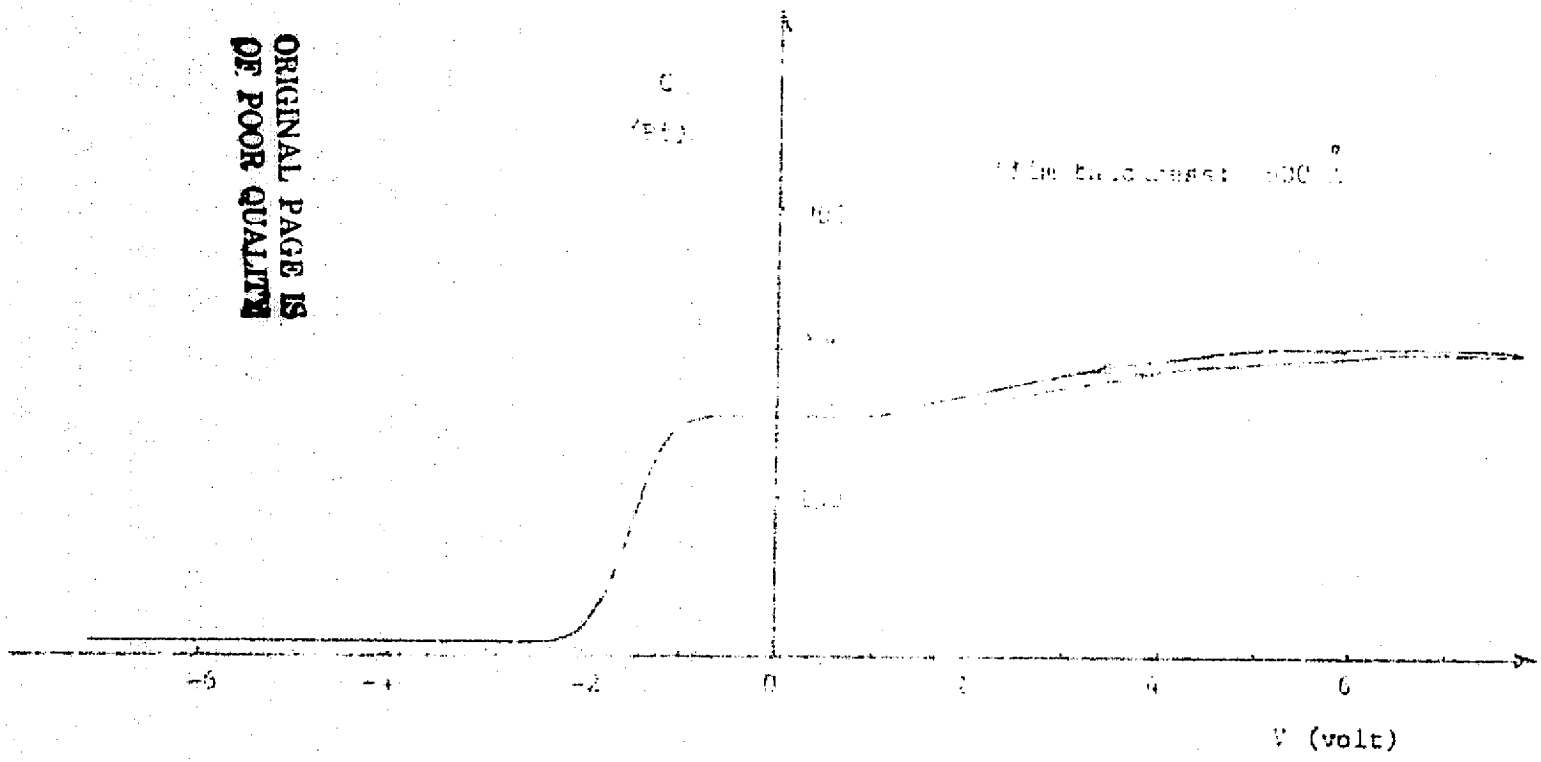

Figure 4.13. The C-V characteristic of an Al-TiO_2-Si MIS capacitor with the TiO_2 films deposited at 200°C

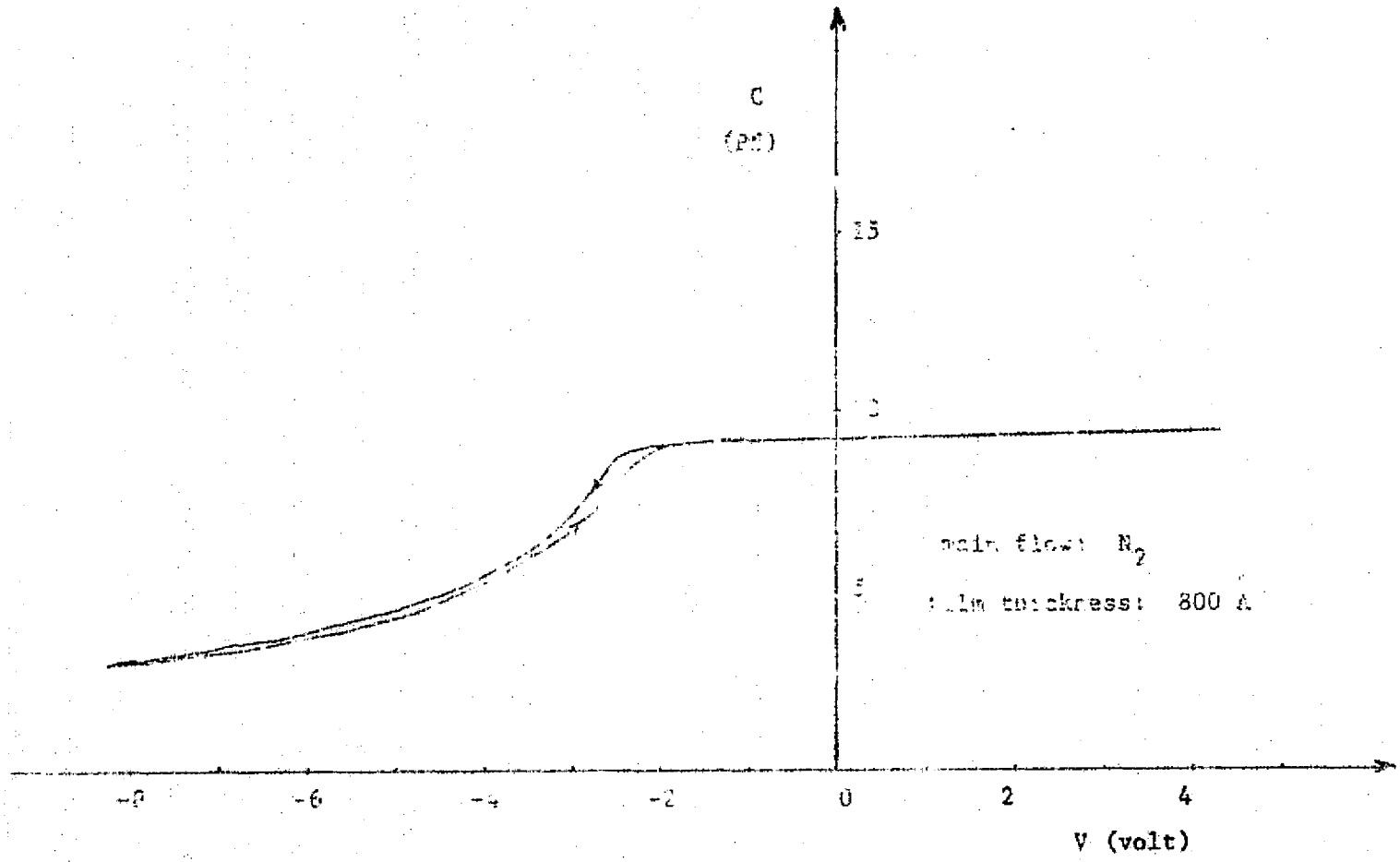

Figure 4.2. The C-V characteristic of an Al-TiO_2-GaAs MIS capacitor with the TiO_2 films deposited at 200°C

at 275°C as shown in Figure 4.21. Because of the fact that TiO_2 film deposited at 275°C can be etched by HF, pattern definition and hence device fabrication are achievable. Altogether, a p- channel depletion mode GaAs MISFET can be built by utilizing the inherent inversion p- channel arising from the built-in negative oxide charges.

Finally, the quantitative results such as dielectric constant, flat-band voltage, and effective fixed oxide charges will be given. Since such a calculation usually requires a strong accumulation capacitance and a strong inversion one as well, only those samples which exhibit strong accumulation and strong inversion will be considered here.

Figure 4.16 shows a C-V curve with a capacitance of 320 pf in strong accumulation. The field plate is an aluminum dot 10 mil (10^{-2} inch) in diameter. The relative dielectric constant calculated from the strong accumulation capacitance is about 50. Substituting Co, C_m, ε_s, N_D, and n_i into Equation (2.32), we obtain a flat-band capacitance of 57 pf. The intersect of the flat-band capacitance with the observed C-V curve provides a flat-band voltage (V_{FB}) of 2.1V. The flat-band voltage is related to the metal-semiconductor work function difference and oxide charge via the following equation [11]

$$V_{FB} = \phi_{MS} - \frac{Q_{SS}}{C_o} - \frac{1}{C_o}\int_0^d \frac{x\rho(x)}{d}\,dx \qquad (4.1)$$

where ϕ_{MS} is the metal-semiconductor work function difference, C_o is the oxide capacitance, Q_{SS} is the fixed oxide charges at the insulator semiconductor interface, $\rho(x)$ is an arbitrary charge distribution per unit area inside the oxide, d is the oxide thickness, and x is measured from the metal-insulator interface. This equation can be written as

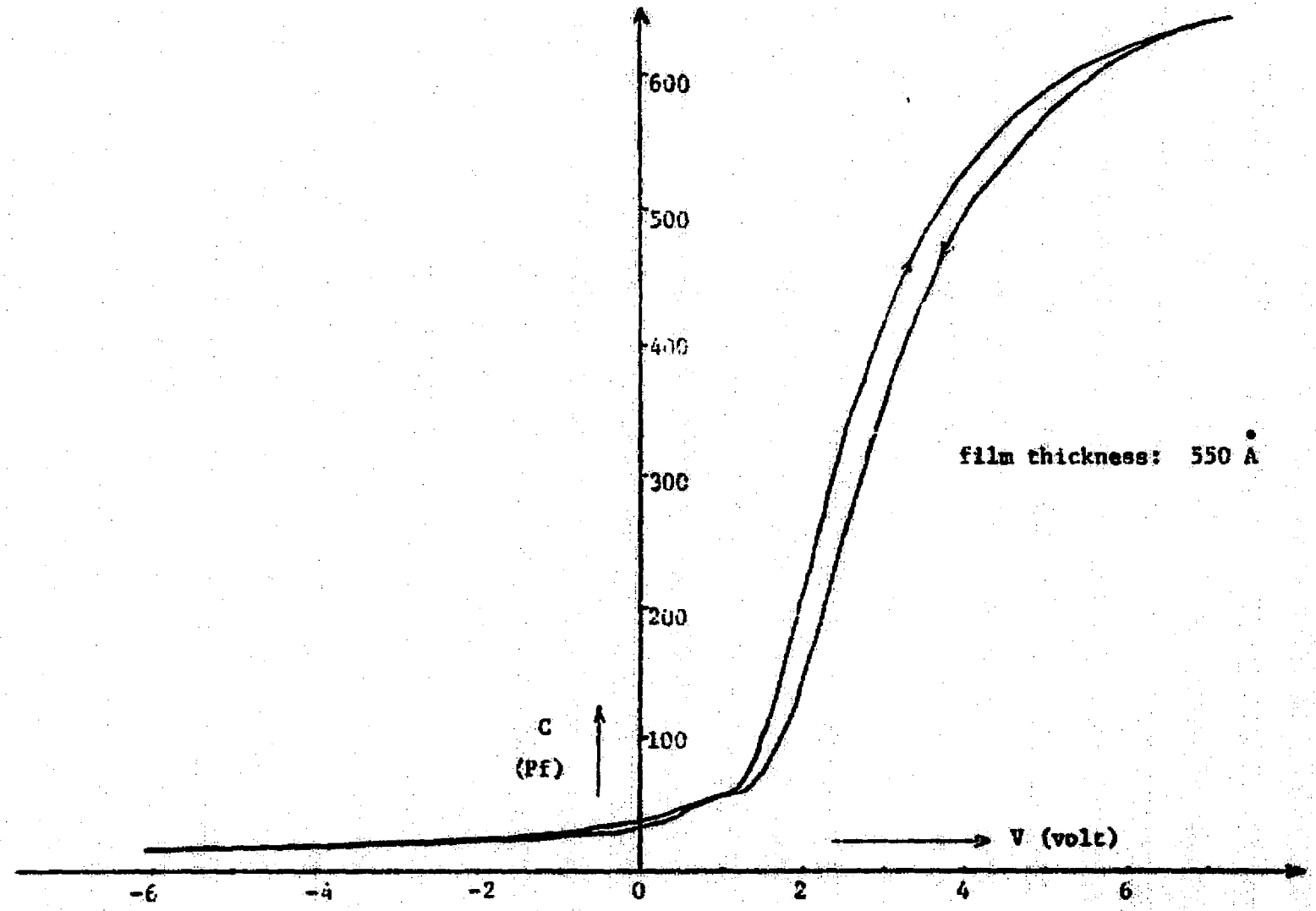

Figure 4.21. The C-V characteristic of an Al-TiO_2-GaAs MIS capacitor with the TiO_2 film deposited at 275°C

$$V_{FB} = Q_{MS} - \frac{Q_{SS,eff}}{C_o} \qquad (4.2)$$

where $Q_{SS,eff} = Q_{SS} + \int_o^d \frac{x\rho(x)}{d}\,dx$ is the effective fixed oxide charges at the insulator-semiconductor interface. Substituting a value of Q_{MS} equal to -0.036V and a V_{FB} of 2.1V into Equation (4.2), one obtains an effective fixed oxide charge of $-1.26\times10^{13}/cm^2$. It is this charge that induces a spontaneous inversion channel in the semiconductor. Although the calculation is performed for one sample only, it is a typical result of the present study.

Based on the result shown in Figure 4.20, one concludes that it is difficult to achieve an inversion layer in the Al-TiO_2-GaAs MIS structure with the TiO_2 films deposited at 200°C. This lack of an inversion layer is usually attributed to either high leakage current or high surface state densities. In spite of the lack of an inversion layer for an Al-TiO_2-GaAs capacitor, an inversion layer can be easily achieved for the Al-TiO_2-Si MIS structure. If the conduction levels of both are assumed to be the same, then one can eliminate the consideration of high leakage current. Therefore, one convinces that high surface state densities make the formation of an inversion layer impossible for the Al-TiO_2-GaAs capacitor with the TiO_2 deposited at 200°C. A theoretical model, based on a similar treatment of Hauser and Bridges [82], will be presented to account for this phenomenon.

Consider a donor-like surface state located somewhere between the mid-gap and the valence band maximum of the n-type GaAs. The energy band diagrams for the donor-like surface states under large positive and negative bias voltage are shown in Figure 4.22. For a large negative

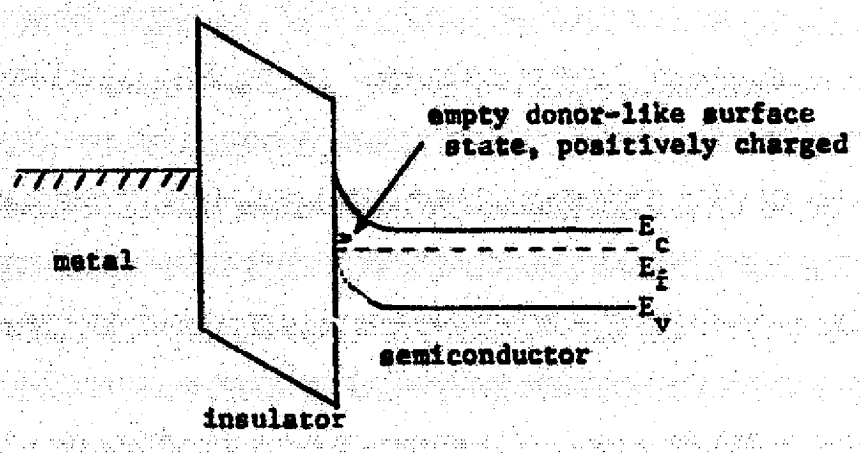

(a) Large negative bias

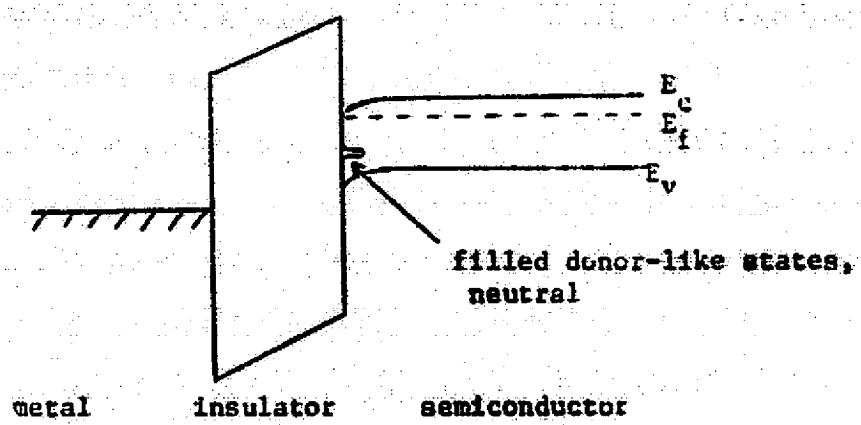

(b) Large positive bias

Figure 4.22. Band diagram of an MIS capacitor at large negative and large positive bias

bias voltage, the donor-like states are unoccupied and are positively charged, while for a large positive voltage the sites are occupied by electrons and are electrically neutral. Due to the dependence of the charge state of the donor-like surface state on the surface potential, the resulting C-V curve will exhibit a plateau somewhere in the depletion region, as shown in Figure 4.23. The width of the plateau ΔV is related to the surface state charges Q_{SS} by

$$\Delta V = \frac{Q_{SS}}{C_o} = \frac{q\, N_{SS}}{C_o} \qquad (4.3)$$

where C_o is the oxide capacitance and N_{SS} is the discrete surface state density in unit states/cm^2. Figure 4.24 shows the C-V curve with a step-like characteristic due to the existence of four discrete surface states. Notice that as the number of the discrete states increase and finally the states are distributed continuously within the forbidden gap, a C-V curve as shown in Figure 4.25 will be observed.

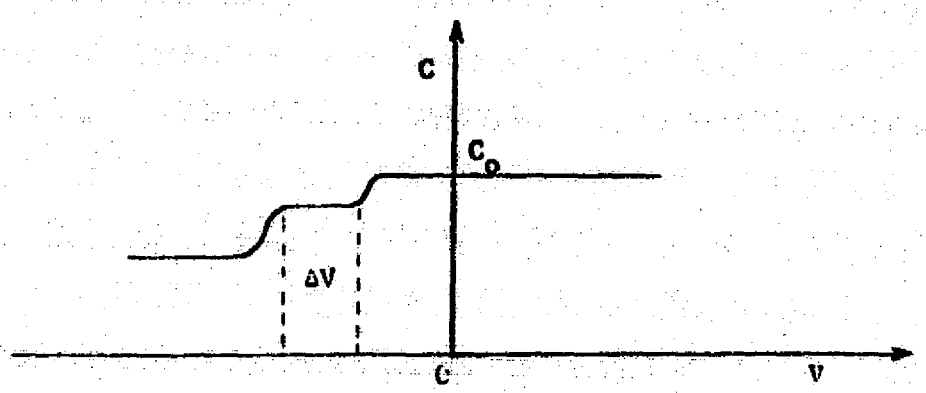

Figure 4.23. The C-V curve of an MIS device with a discrete surface state

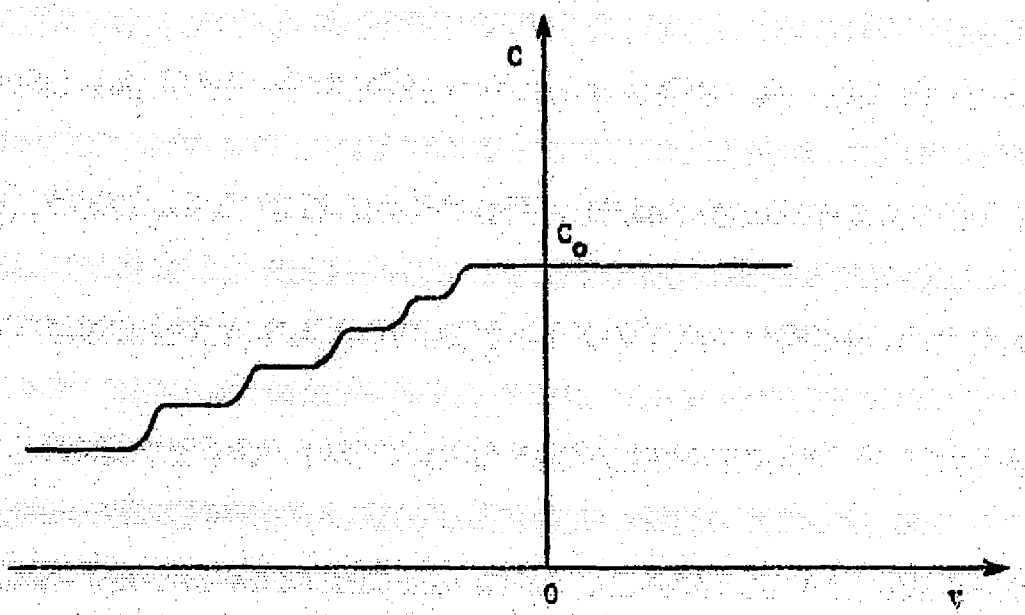

Figure 4.24. The C-V curve of an MIS device with four discrete levels of surface states

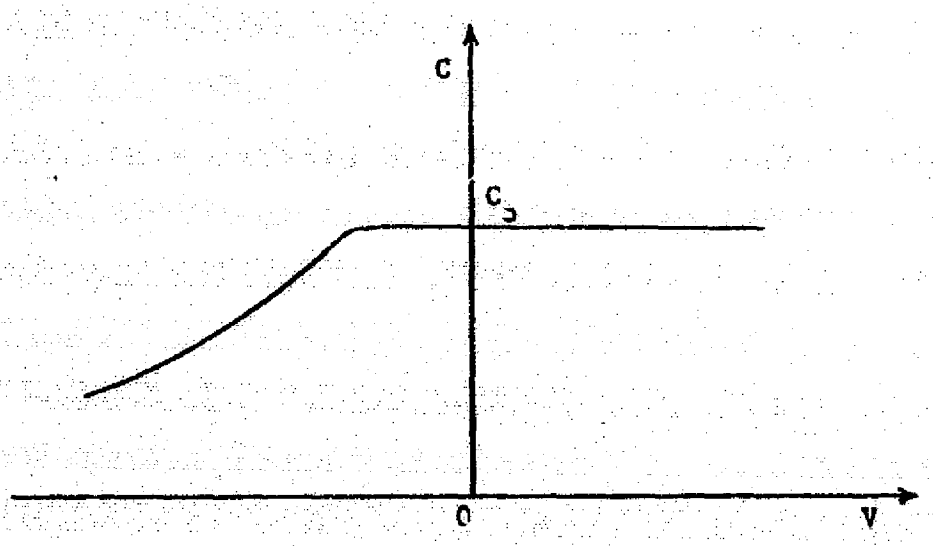

Figure 4.25. The C-V curve of an MIS device with a continuous distribution of the surface states

Consider N_{SS} as a function of the surface potential ψ_S. The voltage change due to the surface state located at the surface potential ψ_S is given by

$$dV = \frac{q\ dN_{SS}(\psi_S)}{C_o} \tag{4.4}$$

If N_{SS} is a continuous function of ψ_S, one can define

$$\frac{dN_{SS}(\psi_S)}{d\ \psi_S} = D \tag{4.5}$$

where D is the surface state densities in states/cm^2-eV. Thus, Equation (4.4) becomes

$$\begin{aligned} dV &= \frac{q\ dN_{SS}}{C_o\ d\psi_S}\ d\psi_S \\ &= \frac{q\ D}{C_o}\ d\psi_S \end{aligned} \tag{4.6}$$

The bias voltage, relative to the flat-band condition, required to obtain an inversion layer is given by integrating Equation (4.6) from $\psi_S = 0$ to $\psi_S = 2\phi_F = 2(E_F - E_i)$, where E_F is the Fermi energy and E_i is the intrinsic Fermi energy [2]. Thus,

$$\begin{aligned} V &= \int dV \\ &= \frac{q}{C_o} \int_o^{2\phi_F} D\ d\psi_S \\ &= \frac{2q\ \bar{D}\ \phi_F}{C_o} \end{aligned} \tag{4.7}$$

where

$$\bar{D} = \frac{1}{2\phi_F} \int_0^{2\phi_F} D \, d\phi_S \qquad (4.8)$$

Based on the result of Equation (4.7), one concludes that an inversion layer is easier to achieve if the dielectric constant is high and the doping level is low. To calculate the tolerable surface state densities for the purpose of achieving an inversion layer at an applied voltage less than 10V, one assumes $C_o = 2\text{x}10^5$ Pf/cm^2 and $\phi_F = 0.7$ eV. Substituting V, C_o and ϕ_F into Equation (4.7), one obtains $\bar{D} = 8.9\text{x}10^{12}$ states/cm^2-eV. However, based on the previous results, one estimates the average surface densities to be in the range of 10^{14} states/cm^2-eV for the Al-TiO_2-GaAs with the TiO_2 films deposited at 200°C if the increase of the surface state densities with the increase of surface potential and the increase of dangling band due to the low oxidation state are considered.

The model discussed above accounts for the difficulty to achieve an inversion layer for the Al-TiO_2-GaAs MIS structure with the TiO_2 films deposited at 200°C and is consistent with the experimental results.

5. SUMMARY, CONCLUSIONS AND RECOMMENDATIONS

Titanium dioxide films prepared by the chemical vapor deposition are investigated in this study as a candidate for the application in the GaAs-MISFET. In order to get a complete insight of the titanium dioxide-gallium arsenide interface, one should study the physical and optical properties of the TiO_2 films first. An ellipsometer, an X-ray diffractometer, and a UV-visible spectrophotometer are among the instruments utilized for these studies. The crystallinity of the TiO_2 films is determined by the deposition temperature and, of course, by the post-deposition heat treatments as well. The as-deposited films are amorphous if the deposition temperature is lower than 275°C, and is polycrystalline anatase phase if the temperature is higher than 400°C. The temperature at 275°C is thought of as a transition temperature between the amorphous and anatase films. Refractive indexes, determined by the ellipsometer, ranges from 1.84 to 2.1, depending on the deposition temperature. It has been observed that the higher the deposition temperatures are, the higher the refractive indexes will be. The polycrystalline TiO_2 films are impervious to most of the chemical etching processes, while the amorphous TiO_2 films can be rapidly etched by dilute hydrofluoric acid. Therefore, low-temperature deposition followed by higher temperature annealing is suggested for devive fabrication. The amorphouse TiO_2 films have a density-of-state gap of 3.2 eV, and the polycrystalline TiO_2 films have a band-gap of 3.76 eV based on a direct band-to-band optical absorption. Such an increase in the band-gap is desirable as far as a barrier for the charge injection from the semiconductor is concerned.

An aluminum-titanium dioxide-aluminum MIM structure is employed for the dc conduction study. The ohmic conduction, which is due to the carrier hopping, is found dominant in the lower voltage region. The Poole-Frenkel emission mechanism is then dominant in the higher voltage region. If the bias voltage is beyond certain value, the d-c conduction is finally dominated by the space-charge limited process. The film deposited at 400°C in a nitrogen atmosphere has a resistivity of 7×10^8 Ω-cm. The resistivity of the TiO_2 film is found to increase the presence of oxygen during deposition. In this case, a resistivity of 6×10^{10} Ω-cm is obtained. These results are in fairly good agreement with those elsewhere.

An aluminum-titanium dioxide-gallium arsenide MIS capacitor is utilized for a capacitance-voltage study. A wealth of results have been obtained based on this study. An inversion layer is usually observed as the film is deposited at a temperature higher than 275°C. A deposition and/or annealing in the oxygen atmosphere is found to be favorable as far as the interface property is concerned. The flat band voltage is positive and on the order of 2.0V, which corresponds to an effective negative oxide charge of $10^{13}/cm^2$ at the TiO_2-GaAs interface. Of technological importance is that an inversion p-type layer is spontaneously built at zero bias voltage. Such a phenomenum is extremely useful in fabricating a p-channel depletion mode GaAs-MISFET since the processes such as shallow diffusion and ion implanation can be eliminated.

Based on the C-V studies, one found that is is difficult to achieve an inversion layer for the Al-TiO_2-GaAs MIS devices with the TiO_2 films deposited at 200°C. A theoretical model, based on the assumption that the surface states are distributed in energy within the forbidden gap, is proposed to interpret this phenomenon. This model reveals that a surface

state density lower than $8 \times 10^{12}/cm^2$-eV is required to achieve an acceptable inversion layer.

Further studies to increase the resistivity of the TiO_2 films and to reduce the surface state densities are suggested. A plasma etching study to solve the etching problem of the TiO_2 films deposited at 400°C is also recommended. An achievement in this respect will make the application of the good quality of the 400°C TiO_2 films to the devices fabrication possible.

In conclusion, this study demonstrates that a p- channel GaAs-MISFET can be successfully fabricated if the good properties of the 400°C TiO_2-GaAs interface can be utilized.

9. LIST OF REFERENCES

1. Richard H. Bube. 1974. Electronic Properties of Crystalline Solids. Academic Press, New York.

2. S. M. Sze. 1969. Physics of Semiconductor Devices. John Wiley and Sons, New York.

3. J. S. Blakemore. 1962. Semiconductor Statistics. Pergamon, Elmsford, New York.

4. H. Becke, R. Hall, and J. White. 1965. Solid-St. Electron 8, 813.

5. W. Kern and J. White. 1970. RCA Rev. 31, 771.

6. T. Miyazaki, et al. 1974. Jap. J. Appl. Phys. Suppl. 2, pt. 2, 441.

7. H. Hasegawa and H. L. Hartnagel. 1976. J. Electrochem. Soc., 123, 713.

8. R.P.H. Chang and A. K. Sinha. 1976. Appl. Phys. Lett., 29, 56.

9. W. D. Brown. 1975. Ph.D. dissertation, University of New Mexico.

10. A. Von Hipple. 1954. Dielectric Materials and Applications. John Wiley and Sons, Inc.

11. A. S. Grove. 1967. Physics and Technology of Semiconductor Devices. John Wiley and Sons, Inc.

12. W. C. Leipold and T. E. Feuchtwang. 1976. J. Non-Cryst. Solids, 21, 181.

13. Frederick Vratny (ed.). 1969. Thin Film Dielectrics. The Electrochem. Soc., Inc., New York.

14. P. J. Harrop and D. S. Campbell. 1968. Thin Solid Films, 2, 273.

15. P. Balk. 1975. J. Electronic Materials, 4, 635.

16. P. K. Ajmera, M. A. Littlejohn, and J. R. Hauser. 1972. J. Electrochem. Soc. 119, 1421.

17. C.A.T. Salama. 1970. J. Electrochem. Soc., 117, 913.

18. J. R. Szedon, et al. 1966. IEEE Solid State Devices. Research Conference, Evanston, Illinois, June.

19. J. R. Szedon and R. M. Handy. 1969. J. Vac. Sci. Technol. 6, 1.

20. C. C. Wang, et al. 1970. RCA Rev., 31, 728.

LIST OF REFERENCES (continued)

21. E. Kaplan, et al. 1976. J. Electrochem. Soc., 123, 1570.

22. E. T. Fitzgibbons, et al. 1972. J. Electrochem. Soc., 119, 735.

23. K. G. Geraghty, et al. 1976. J. Electrochem. Soc., 123, 1201.

24. Y. Sato. 1968. Jap. J. Appl. Phys., 7, 595.

25. J. E. Foster and J. M. Swartz. 1970. J. Electrochem. Soc., 117, 1384.

26. J. A. Cooper, Jr., et al. 1972. Solid-St. Electron., 15, 1219.

27. T. Ito and Y. Sakai. 1973. Trans. Inst. Elect. Eng. Jpn., 93-A, 11.

28. G. D. Bagratishvili, et al. 1976. Phy. Stat. Sol. (a), 36, 73.

29. S. P. Murarka. 1975. Appl. Phys. Lett., 26, 180.

30. R. A. Logan, B. Schwartz, and W. J. Sundburg. 1973. J. Electrochem. Soc., 120, 1385.

31. H. Hasegawa, et al. 1975. Appl. Phys. Lett., 26, 567.

32. K. H. Zaininger. 1968. RCA Engr., 15, 50.

33. T. Ito and Y. Sakai. 1974. Solid-St. Electron., 17, 751.

34. A. G. Revesz and K. H. Zaininger. 1963. J. Am. Gerem. Soc., 16, 606.

35. J. Frenkel. 1938. Phys. Rev. 54, 657.

36. R. M. Hill. 1967. Thin Solid Films, 1, 39.

37. A. K. Jonscher. 1967. Thin Solid Films, 1, 213.

38. J. G. Simmons, 1971. J. Phys. (D), 4, 613.

39. P. L. Young. 1976. J. Appl. Phys. 47, 235 and 242.

40. W. Schottky. 1914. Z. Phys., 15, 872.

41. W. E. Flannery and S. R. Pollack. 1967. J. Appl. Phys., 37, 4417.

42. C. A. Mead. 1962. Phys. Rev., 128, 2088.

43. B. Lalevic and G. Taylor. 1975. J. Appl. Phys., 46, 3208.

44. S. Wang. 1966. Solid State Electronics. McGraw-Hill.

LIST OF REFERENCES (continued)

45. J. R. Yeargan and H. L. Taylor. 1968. J. Appl. Phys., 39, 5600.

46. N. S. Saks. 1975. Solid-St. Electron., 18, 737.

47. L. M. Terman. 1962. Solid-St. Electron., 5, 285.

48. K. Lehovec. 1968. Solid-St. Electron., 11, 135.

49. C. N. Berglund. 1966. IEEE Trans. El. Dev., ED-13, 701.

50. M. Kuhn. 1970. Solid-St. Electron., 13, 873.

51. E. H. Nicollian and A. Goetzberger. 1967. Bell Syst. Tech. J., 46, 1055.

52. G. Declerck, et al. 1973. Solid-St. Electron., 16, 1451.

53. K. H. Zaininger and G. Warfield. 1965. IEEE, Trans. Electron Devices, ED-12, 179.

54. K. Lehovec and A. Slobodskoy. 1964. Solid-St. Electron., 7, 59.

55. P. G. Lecomber and J. Mort, (eds.) 1973. Electronic and Structural Properties of Amorphous Semiconductors. Academic Press, New York.

56. N. F. Mott. 1967. Adv. Phys., 16, 49.

57. M. H. Cohen, H. Fritzsche, and S. R. Ovshinsky. 1969. Phys. Rev. Lett., 22, 1065.

58. J. Tauc and A. Menth. 1972. J. Non-Cryst. Solids, 8-10, 569.

59. C. F. Powell, et al. 1966. Vapor Deposition. John Wiley and Sons, Inc., New York.

60. S. M. Sze. 1974. Integrated Circuit Technology. (private communication)

61. C. C. Chang, P. H. Citrin, and B. Schwartz. (To be published in J. Vac. Sci. Technol.)

62. P. Kofstad. 1962. J. Phys. Chem. Solids, 23.

63. V. L. Rideout. 1975. Solid-St. Electron., 18, 541.

64. E. A. Davis and N. F. Mott. 1970. Phil. Mag., 22, 903.

65. K. H. Zaininger and A. G. Revesz. 1964. RCA Review, 25, 85.

66. R. J. Archer. 1968. Ellipsometry. Gaertner Scientific Corp.

LIST OF REFERENCES (continued)

67. F. L. McCrackin, et al 1963. J Res. Natl. Bur. Std., 67A, 363.

68. F. L. McCrackin, et al. 1969. Technical Note No. 479, Natl. Bur. Std.

69. J. Tauc. 1969. Optical Properties of Solids, edited by S. Nudelman and S. S. Mitra, Plenum Press, New York.

70. G. R. Fowles, 1972, Introduction to Modern Optics, Holt, Rinehart, and Winston, Inc.

71. J. M. Woodall and H. J. Hovel. 1977. Appl. Phys. Lett., 30, 492.

72. J. R. Devore. 1951. J. Opt. Soc. Am. 41, No. 6.

73. J. Maserjian and C. A. Mead. 1967. J. Phys. Chem. Solids, 28, 1971.

74. M. Duffy, et al. 1968. J. Electrochem. Soc., 115, 61C.

75. M. Yokozawa, et al. 1968. Jap. J. Appl. Phys., 7, 96.

76. N. Daude, et al. 1977. Phys. Rev. B, 15, 3229.

77. A. Miller and E. Abrahams. 1966. Phys. Rev., 120, 745.

78. F. A. Grant. 1959. Rev. Modern Phys., 31.

79. L. E. Hollander, Jr. and P. L. Castro. 1962. J. Appl. Phys., 23, No. 12.

80. T. Hada, et al. 1976. Jap. J. Appl. Phys., 9, 1078.

81. B. E. Deal, et al. 1968. J. Electrochem. Soc., 115, 300.

82. J. R. Hauser and J. R. Bridges. 1966 Annual Progress Report, NASA Grant NSG-588.